Automated fabrication of a scalable heart-on-a-chip device by 3D printing of thermoplastic elastomer nanocomposite and hot embossing

Qinghua Wu [a,b], Ruikang Xue [c], Yimu Zhao [b], Kaitlyn Ramsay [a], Erika Yan Wang [d], Houman Savoji [f,g,h], Teodor Veres [i,j], Sarah H. Cartmell [c], Milica Radisic [a,b,e,k,*]

[a] Institute of Biomedical Engineering, University of Toronto, Toronto, Ontario, M5S 3G9, Canada
[b] Toronto General Research Institute, University Health Network, Toronto, Ontario, M5G 2C4, Canada
[c] Department of Materials, School of Natural Sciences, Faculty of Science and Engineering and The Henry Royce Institute, Royce Hub Building, The University of Manchester, Manchester, UK
[d] Koch Institute for Integrative Cancer Research, Massachusetts Institute of Technology, Cambridge, MA, 02139, USA
[e] Department of Chemical Engineering and Applied Chemistry, University of Toronto, Toronto, Ontario, M5S 3E5, Canada
[f] Institute of Biomedical Engineering and Department of Pharmacology and Physiology, University of Montreal, Montreal, Quebec, H3T 1J4, Canada
[g] Research Center, Centre Hospitalier Universitaire Sainte-Justine, Montreal, Quebec, H3T 1C5, Canada
[h] Montreal TransMedTech Institute, Montreal, Quebec, H3T 1J4, Canada
[i] National Research Council of Canada, Boucherville, QC, J4B 6Y4, Canada
[j] Department of Mechanical and Industrial Engineering, University of Toronto, Toronto, Ontario, M5S 3G8, Canada
[k] Terrence Donnelly Centre for Cellular & Biomolecular Research, University of Toronto, Toronto, ON, M5S 3E1, Canada

ARTICLE INFO

ABSTRACT

The successful translation of organ-on-a-chip devices requires the development of an automated workflow for device fabrication, which is challenged by the need for precise deposition of multiple classes of materials in micro-meter scaled configurations. Many current heart-on-a-chip devices are produced manually, requiring the expertise and dexterity of skilled operators. Here, we devised an automated and scalable fabrication method to engineer a Biowire II multiwell platform to generate human iPSC-derived cardiac tissues. This high-throughput heart-on-a-chip platform incorporated fluorescent nanocomposite microwires as force sensors, produced from quantum dots and thermoplastic elastomer, and 3D printed on top of a polystyrene tissue culture base patterned by hot embossing. An array of *built-in* carbon electrodes was embedded in a single step into the base, flanking the microwells on both sides. The facile and rapid 3D printing approach efficiently and seamlessly scaled up the Biowire II system from an 8-well chip to a 24-well and a 96-well format, resulting in an increase of platform fabrication efficiency by 17,5000–69,000% per well. The device's compatibility with long-term electrical stimulation in each well facilitated the targeted generation of mature human iPSC-derived cardiac tissues, evident through a positive force-frequency relationship, post-rest potentiation, and well-aligned sarcomeric apparatus. This system's ease of use and its capacity to gauge drug responses in matured cardiac tissue make it a powerful and reliable platform for rapid preclinical drug screening and development.

1. Introduction

The pharmaceutical industry confronts unprecedented challenges in its quest to reduce costs and improve the efficiency and accuracy of drug development [1]. Recent advances in microfabrication, microfluidics, and stem cell biology have enabled close recapitulation of pertinent features of human physiology *in vitro* in miniaturized platforms (colloquially called "chips"), to model functions of organs such as the kidney [2], brain [3], liver [4] and heart [5]. These advances hold the potential to substantially enhance the predictive power of current preclinical and clinical evaluations [6–16].

Recent heart-on-a-chip studies have enabled both cardiac drug testing and disease modelling, by improving the maturation of cardiac tissue derived from human induced pluripotent stem cells (iPSCs) and

providing integrated physiological readouts such as contractility, calcium handling and electrophysiology [5,17–20]. They generally describe the development of cylindrical structures of human ventricular myocardium from iPSC-derived cardiomyocytes, with a diameter of several hundred micrometers, anchored to two ends of the organ-on-a-chip platform [5,5,21,22]. Contractile dynamics such as beating frequency can be evaluated via the optical analysis of cardiac tissue displacement [15,23–25]. Either the deflection of polydimethylsiloxane (PDMS) posts [8,26], or elastomeric polymer wires as in the Biowire II device [27], can be used to quantify the contraction force of these tissues in response to the applied drugs or as a result of genetic mutations of the cardiomyocytes. Ideally, these measurements are performed under electrical pacing due to the force-frequency relationship of the adult heart muscle that may confound the drug effects on contractile force and rate [27]. Additionally, there is an incentive to grow heart tissues suspended above the culture substrate, as the presence of the tissue contact with the rigid plastic substrate may prevent the accurate evaluation of contractile dynamics and hinder tissue maturation due to the unphysiologically high substrate stiffness.

Yet the mainstream application of heart-on-a-chip systems requires compatibility with standard pharmaceutical workflows that almost exclusively rely on liquid handling robots and high-content imaging stations. This equipment requires devices with a footprint of multiwell plates, produced from standard materials, such as tissue culture polystyrene in a scalable fashion. In our earlier work [20], we introduced a heart-on-a-chip device in a well-plate format. However, this approach had limitations, mainly because of two factors. Firstly, it involved manual manipulation of PDMS molds and elastomeric polymer wires, leading to a low production throughput. Secondly, the process required considerable time for crosslinking and molding, further affecting the efficiency of the production process.

Here we sought to develop a scalable approach for the fabrication of multiwell plate-based heart-on-a-chip devices with automated deposition of both elastic microwires for tissue anchoring and force sensing, as well as carbon electrodes for field stimulation. We chose to rely on 3D printing as a low-cost, highly versatile, easily scalable and efficient modality for the placement of flexible suspended sensing elements in combination with hot embossing of polystyrene for the fabrication of multiwell structures with integrated electrodes. Thermoplastic elastomers (TPE) feature flexibility, tunable elasticity, low-absorption, ease of molding, and biocompatibility. Thus, they can be easily applied in extrusion-based 3D printing [28,29], such as in the fabrication of microwires that serve as tissue anchor points and force sensors in Biowire II heart-on-a-chip devices. However, a limitation of TPE is its lack of autofluorescence, making it challenging to accurately track wire displacement. Owing to the multifaceted properties such as photoluminescence [30], high photostability [31] and long fluorescence lifetime [32,33], semiconductor quantum dots (QDs) have been used as optical nanoplatforms for cell imaging [34] and represent an ideal candidate for the implementation of fluorescent microwires here.

We hypothesize here that a nanocomposite consisting of a TPE elastomer and QDs, will be suitable for automated fabrication via 3D printing of elastic wires that will act as anchor points for cardiac tissue cultivation and force sensing. Here, we demonstrated the automated integration of *built-in* conductive carbon electrodes and TPE/QD nanocomposite microwires into multiwell plate devices for long-term electrical conditioning, stimulation and *in situ* contractile evaluation. The electrical field distribution in various multiwell devices was mathematically modelled to optimize electrode position and well format to ensure a uniform electrical field for tissue culture. The approach has demonstrated a significant reduction in the time of manufacturing per well of each device, thus increasing the fabrication efficiency by 17,5000–69,000% compared to our previously described and commercialized Biowire II platform that relies on polyester elastomer microwires [5,20].

2. Materials and methods

2.1. TPE/QD ink preparation

The nanocomposites were prepared by mixing core-shell CdSe/ZnS quantum dots (QDs) (1 mg/mL in toluene, Sigma-Aldrich) and poly (styrene) (ethylene/butylene)–(styrene) copolymer (SEBS) (Versaflex CL30, PolyOne, Viscosity of 14800 cP at shear rate of 11200 S^{-1} at 200 °C). In brief, the TPE polymer was mixed with QDs separately (λ_{em} 450 nm and λ_{em} 630 nm, separately, from Sigma-Aldrich) in toluene to generate the nanocomposite at a concentration of 0.05 w/w% QDs in the polymer. The nanocomposite solutions were cast into a glass Petri dish (Fisher Scientific). After solvent evaporation overnight under ambient conditions, the nanocomposite inks were then baked in an oven under a vacuum at 75 °C, for 2 h.

2.2. Fabrication of base plate with built-in carbon electrodes

Photolithography was applied to fabricate a SU-8 photoresist master mold generated using a photomask. Pattern designed by AutoCAD was used to produce the photomask, with repeated rectangular microwells ($5 \times 1 \times 0.3$ mm^3, length (L) × width (W) × height (H)) and grooves (75 $\times$ 0.2 mm^2, $L \times W$). The distances between adjacent microwells in the patterns were adjusted to ensure compatibility with the 24-well and 96-well plate dimensions. A negative (polydimethylsiloxane (PDMS) mold was produced by mixing a silicone elastomer base and a curing agent at a weight ratio of 5:1 (Sylgard 184 silicone elastomer kit, Dow Corning, cat. no. 3097358-1004) and pouring the mixture onto the SU-8 master mold. The sample was allowed to cure at room temperature. The PDMS mold was then fixed to a silicon wafer via plasma bonding, by a plasma generator (handheld, BD-20AC Laboratory Corona Treater, Electro-Technic Products) to serve as a mold for hot embossing of tissue culture polystyrene. In brief, a blank polystyrene sheet and carbon electrodes (Cat No. AR-14, Ohio Carbon Blank) were placed closely on both sides of the microwell pattern on the PDMS mold affixed to the silicon wafer and loaded into a hot embosser (EVG 520, EV Group). The polystyrene base plate with built-in carbon electrodes was generated by hot embossing the polystyrene sheet against the PDMS mold at a temperature of 180 °C and a pressing force of 3000 N, for approximately 30min per base plate.

2.3. 3D printing of TPE/QD nanocomposite microwires

The nanocomposite material was loaded into a temperature-controlled vat of a 3D bioprinter (RegenHU Ltd., Switzerland). The TPE/QD nanocomposite ink was extruded through a 60 µm micronozzle and deposited on a three-axis positioning platform, at 210 °C and 0.01–0.4 MPa with a controllable robot velocity of 1–5 mm s^{-1}. An array of nanocomposite micro-wires (73 mm × 94.5 mm × 60 µm, $L \times W \times D$ (diameter) for a 24 well-format; 72 mm × 99 mm × 60 µm for a 96 well-format) was directly deposited on the polystyrene base plate embedded with electrodes.

2.4. Fabrication of multiwell plate devices

A polystyrene plate base with electrodes and TPE/QD nanocomposite microwires was assembled onto a bottomless 24-well plate or 96-well plate, by thermal bonding, using a heated press device (Carver 4386), for 5 min, at a pressing force of 500 bar and a temperature of 120 °C. In brief, the bottomless 24-well plate (base up) was placed on the bottom plate of the press device. The base plate with microwires and electrodes was placed on top of the bottomless plate, with the nanocomposite microwires aligned in the center of the wells. Polyurethane glue (two-part adhesive casting system; GS Polymers, cat. No. 1552-2T50) was additionally used to glue the connection between the part of electrodes in the base and the bottomless plate and baked in an oven

at 75 °C, for 2 h. The application of small amount of glue to the connection points as described, ensures that the device remains leak free. The whole plate with the embedded nanocomposite wires was imaged using a Keyence Digital Microscope (Keyence VHX7000). A control device consisted of the standard Biowire II platform, consisting of a strip of 8 microwells positioned between two carbon electrodes (1/ 8" Ladd Research Industries) that are spaced 1 cm apart in a 10 cm Petri dish as we described in detail previously [27,35]. Briefly, the microwell strip was also engineered from tissue culture polystyrene, with an identical configuration to that of the plate devices, with 100 μm diameter wires produced from polyester elastomer poly (octamethylene maleate (anhydride) citrate) (POMaC). POMaC was generated by a single pot melt polymerization of citric acid, maleic anhydride, and 1, 8-octanediol, and the wires were generated by casting in PDMS molds as we described previously [35]. POMaC wires were manually inserted into the polystyrene strips as we described [35]. Specifically, a polystyrene base with repeating rectangular microwells (5 mm × 1 mm × 300 μm, L × W × H) and two parallel grooves (200 μm × 100 μm, W × H) was generated by hot embossing from a SU-8 mold designed using AutoCAD. The polystyrene base was then cut into strips containing 8 microwells. A SU-8 photoresist master mold with only grooves (100 μm × 80 mm, W × H) was used to produce a negative polydimethylsiloxane (PDMS) master mold (Zhang et al., 2016). The PDMS master was used to hot emboss the microwells into a polystyrene sheet a negative mold for generating POMaC wires was obtained by pouring PDMS (Sylgard 184 silicone elastomer kit, 1:10 ratio of crosslinker to elastomer) on a SU-8 photoresist master fabricated by photolithography. The Biowire II device can be sterilized by a gamma irradiation process. The PDMS mold was then lightly attached to a glass slide, followed by the perfusion of POMaC pre-polymer solution through the microchannels on the mold by capillary force. The mold with the pre-polymer solution was cured by UV exposure (5100 mJ/cm^2). The POMaC wires were then immersed in phosphate-buffered saline (PBS, Gibco, cat. no. 14190-144) to pealing them off from the glass slide. The wires were manually placed into the two parallel grooves on the polystyrene strips. Polyurethane 2-part adhesive (SP 1552–2, GS Polymers, Inc.) was used in a minimal quantity to fix the POMaC wires on the strips. The strips were placed into a customized chamber with two 1/8 inch-diameter carbon rods (Ladd Research Industries) 1 cm apart (inner edge-to-inner edge) to the bottom of a 10 cm tissue culture dish. 15 mL of culture media was added into the Petri dish for cell culture. The Biowire II device can be sterilized by a gamma irradiation process.

To calculate the cost per well for a Biowire II device the costs were estimated as follows: carbon rods ($11.7, 24-inch, 1/8 inch-diameter); Petri dish ($3.65/20 unit); monomers for POMaC wire synthesis: 1,8-octanediol ($153/100 g), citric acid $53.3/100 g), maleic anhydride ($29/100 g). To calculate the cost per well for each multi-well device: carbon electrodes ($90.2/24 piece), 24-well bottomless plate ($89/28 unit), 96-well bottomless plate ($58/10 unit), quantum dots ($195/1 mL, 10 mg/mL), SEBS ($73/10 Kg), to reach 0.05 w/w% of QD in the SEBS for the nanocomposites. For both devices: polystyrene sheet ($33.6, 24 inch × 24 inch) and platinum wires ($200/10 ft). Labor time (a technician working $70,000/year), approximately 12 h of work for POMaC synthesis and around 1 h for TPE/QD nanocomposites; approximately 28.5 h labor time to generate 96 total wells for Biowire II devices and around 1.4 h for generating one multiwell plate.

2.5. Swelling properties

The swelling properties of POMaC and TPE/QD wires were examined by immersing the wires into distilled water, PBS and I3M culture media for 24 h. The wire diameter before and after immersing into different solutions was observed by using an Olympus IX81 inverted microscope.

2.6. Nanocomposite microwire force-displacement curves

The force-displacement curves of TPE and TPE/QD microwires (diameters of 100 μm) were measured using a microscale mechanical tester (MicroSquisher, CellScale) (Fig. S1A). Customized tips (half ellipse, 4:1 diameter ratio, long diameter of the half ellipse: 500 μm, 700 μm, and 800 μm, separately), generated from SU-8 molds by photolithography, were adhered to the tungsten probe (0.1524 mm) using an adhesive glue (T-GSG-01 Titan Gel) to mimic the curvature and diameter of tissues on the wires. Each probe tip was placed in the middle of the nanocomposite wire in the microwell and moved forward at a velocity of 2.5 μm/s, while the force was applied perpendicular to the long axis of the wire. The probe displacement, time and force were recorded, and force-displacement curves were generated. Prism 9.0 was used for data analysis and for generating fitted curves, 95% confidence interval curves and R^2 values.

2.7. Young's modulus measurement

Dog-bone-shaped TPE/QD samples (with the inner strip dimensions: width of 5 mm, thickness of 3 mm and length of 25 mm) were generated by injection molding (DSM IM5.5, DSM Netherlands). The mechanical testing was performed using an Electroforce 5200 Biodynamic Test Instrument (BOSE) with a strain rate of 0.1 mm s^{-1}, to reach a strain of 120%. The mechanical data were obtained using WinTest software. Young's modulus was calculated from the data within the first 20% of strain.

2.8. Finite element modelling of the electric field distribution

Electric field distribution in different culture systems (i.e., 10 cm dish, 24-, 96- and 384-well plates) was simulated with COMSOL Multiphysics 5.1 (COMSOL, UK). Each finite element (FE) model was composed of a standard-sized polystyrene culture well, two carbon electrodes, culture medium, two TPE microwires and a hydrogel. The 10 cm dish model also included two platinum wires which were connected to the electrodes. The material properties applied in the model can be found in Table S1. The Electric Currents interface of the software, which solves a current conservation equation based on Ohm's law, was used. The equation included the scalar electric potential as the dependent variable and considered the inductive effects to be negligible. One electrode was set as ground, which had 0 V terminal voltage. Terminal voltages of 5 V and 2.5 V were applied to the other electrode in the dish and well-plate models, respectively, resulting in a potential difference of 500 V/m. Meshes containing tetrahedral elements with adaptive element size were automatically generated with physics-controlled mesh and Finer element size settings of the software. A stationary study step was created and the electric field distributions were visualized.

2.9. Generation of engineered cardiac tissues

Human induced pluripotent stem cells (hiPSC) cardiomyocytes (CMs) were differentiated from hiPSC line BJ1D (a kind gift from William Stanford, Ottawa Hospital-Institute Research) by monolayer differentiation protocols [36,37] as we described [27]. The CMs monolayers were dissociated into single cells on day 18 of stem cell differentiation, using previously described methods [37]. The disassociated cells and cardiac fibroblasts (Lonza, NHCF-V) were mixed at a cell count ratio of 10:1 and then remixed in a collagen hydrogel (6×10^7 cells/mL). The collagen hydrogel (500 μL) was obtained by mixing rat tail collagen (153 μL at 9.82 mg/mL, Corning), 1X M199 (50 μL, Sigma), Matrigel (75 μL, BD Biosciences), NaHCO$_3$ (50 μL at 26 mM, Sigma), deionized sterile water (167 μL) and NaOH (5 μL at 1 M, Sigma). Before cell seeding, each well was treated with 5% (w/v) pluronic acid (Sigma-Aldrich) for 10min, followed by PBS wash. The cell-laden hydrogel

was seeded in the microwells of the plate (2 μL per microwell). The plate was then incubated at 37 °C and 5% CO_2 for 10 min to allow for hydrogel gelation, after which, 2 mL Induction 3 Medium (I3M) (StemPro-34 complete media, 20 mM HEPES, 1% GlutaMAX, 1% penicillin-streptomycin, Life Technologies; 213 μg/mL 2-phosphate ascorbic acid, Sigma-Aldrich) were added to each well. After cell-laden gel seeding, the tissues were incubated for 7 days, followed by tissue culture for four weeks under electrical stimulation. The culture media was changed every week during the period of five weeks. Tissue morphology was observed daily for one week after cell seeding using an Olympus IX81 inverted microscope.

2.10. Cytotoxicity assessment

The neonatal rat heart cells were isolated from neonatal rats as described previously [38], according to an approved protocol by the University of Toronto Animal Care committee [39]. Sprague Dawley neonatal rats (one to two days old) were euthanized. The hearts were obtained and quartered and rinsed in HBSS. According to the manufacturer's protocol, digestion was performed using GentleMACS Dissociator (Miltenyi Biotec) and Neonatal Heart Dissociation Kit. Cells after digestion were incubated for 1 h and collected for further cell seeding. The rat CMs and cardiac fibroblasts (Lonza, NHCF-V) were mixed at a cell count ratio of 10:1 and then remixed in a collagen hydrogel (6×10^7 cells/mL). The hydrogel was prepared as described above. The cell-laden hydrogel was seeded in the microwells of the 24-well plate device (fabricated with TPE and TPE/QD microwires, separately) and Biowire II device with PoMAC microwires (2 μL per microwell). After placing a droplet of the medium on the wall of the well to maintain moisture, the plate was incubated at 37 °C and 5% CO_2 for 10 min to allow for hydrogel gelation. 2 mL Dulbecco's modified Eagle's medium (4.5 g/L glucose, 10% v/v FBS, 1% v/v penicillin-streptomycin (100 mg/mL), 1% v/v HEPES (100 U/mL), and 1% GlutaMax supplement) was added to each well. After tissue culture of two weeks, cardiac tissues from both devices were stained with carboxyfluorescein diacetate succinimidyl ester (CFDA-SE, 1:1000) and propidium iodide (PI, 1:75) in DPBS at 37 °C for 30 min. After rinsing the tissues with DPBS three times, the tissues were fixed in 4% formaldehyde for 30 min at room temperature. Fluorescent images of the tissues were captured by an Olympus IX81 inverted microscope.

2.11. Electrical stimulation

The carbon electrodes along the microwells in the 24-well plate device were connected to an external electrical stimulator (Grass Technology S88X Square Pulse Stimulator). To induce tissue maturation, samples were electrically stimulated starting at 1 or 2 Hz based on whether the tissue was captured at that stimulation frequency, with a 1 Hz weekly increase in frequency for a total period of 4 weeks. Biphasic stimulation (1 ms pulse duration per phase) at 1 Hz was applied during electrical stimulation. The stimulation was initiated at 1 Hz or 2 Hz, depending on the frequency that the tissues can catch. The stimulation voltage was adjusted weekly to 1.5 times the average excitation threshold (ET). ET was defined as the minimum voltage required for synchronous tissue pacing and it was determined at 1 Hz. Maximum capture rate (MCR) was defined as the maximum pacing frequency under electrical stimulation at 2 times of the ET.

2.12. Force recording and analysis

The bright-field videos of cardiac tissues from well plate devices were recorded in the chamber (37 °C, 5% CO_2) of the fluorescence microscope (Olympus CKX41 inverted microscope) under 4× objective. Force calculations over five weeks were performed based on data collected from the bright-field videos and red fluorescence videos. The minimum voltage per cm (excitation threshold, ET) required to cause

synchronized contraction of the cardiac tissue was measured by observing tissue displacement via the microscope under electrical stimulation at 1 Hz generated by an external stimulator (Grass Technology S88X Square Pulse Stimulator). The maximum capture rate (MCR) of the cardiac tissues was measured by stimulating the tissue at a voltage of 2 times the ET and increasing the stimulation frequency to the frequency value required for the tissues to lose the synchronized beating. The displacement of the fluorescent polymer wires was recorded under a 10× objective to monitor spontaneous beating without stimulation and stimulated beating of tissues under electrical stimulation at a voltage of 2 times the ET, from 1 Hz to 3 Hz (10 s for each frequency), followed by ceasing stimulation for 10 s and stimulating again at 1 Hz for 10 s. The videos were analyzed using custom MATLAB software, as described previously [5]. The bright-field images of tissues cultured in the well-plate devices over a week after cell seeding were taken under 4× objective in the chamber (37 °C, 5% CO_2) of the fluorescence microscope (Olympus IX81 inverted microscope).

Briefly, force calculations for the tissues were examined using the bright-field videos to assess tissue diameter as well as red fluorescence videos to collect wire displacement during tissue contraction as we previously described [27] (Fig. S1B). The red fluorescence videos of the tissues observed by the fluorescence microscope were recorded to examine the displacement of fluorescent polymer wires as a result of cardiac tissue contraction at a frame rate of 100 frame/s, under a 10 × objective in the Texas Red channel ($\lambda_{ex} = 596$ nm, $\lambda_{em} = 620$ nm), under the spontaneous beating and stimulated beating of tissues by electrical stimulation at a voltage of 2 times the ET at 1 Hz, separately. The fluorescence videos were converted to stacks of still frames for analyzing the tissue contraction. The maximum (at the maximum contraction of the tissue) and minimum (at the relaxed state of the tissue) wire deflections were evaluated at the center of the wire were converted to force measurements, by using the calibration curves from force-displacement equations by different customized tips as described previously [40]. Specifically, this was achieved by measuring the displacement of the nanocomposite wire due to tissue contraction from the fluorescence videos and using the calibration generated with a tip diameter that best corresponds to the tissue diameter (average tissue width) on the wire using a customized MATLAB code as we previously described [27,41]. The tissue diameter and width of the tissues wrapped around the nanocomposite wires were observed from still frames of the 4 × bright-field videos of the tissues in the relaxed position. The active force of the tissue was defined here as the force value between the maximum (total) force and the force evaluated at the minimum wire displacement (defined as passive tension).

2.13. Immunostaining and confocal microscopy

After 4-week stimulation (5 weeks of tissue culture in total) in 24-well plate device, the tissues were fixed with 4% paraformaldehyde, permeabilized with 1% Triton X, and blocked with 5% bovine serum albumin (BSA). Samples were immunostained with mouse anti-cardiac Troponin T (ThermoFisher; 1:200) and then with donkey anti-mouse-Alexa Fluor 488 (Abcam; 1:400) antibodies. Phalloidin-Alexa Fluor 660 (Invitrogen; 1:200) was used to stain F-actin fibers. Confocal fluorescence microscopy images were captured using an Olympus FluoView 1000 laser scanning confocal microscope.

2.14. Drug testing

At week 5 after cell seeding, Ca^{2+} dye fluo-4 NW (Thermo Fisher) was added to each well of the 24-well plates, followed by incubation for 30 min at 37 °C prior to the drug testing. Recordings were performed in the environmental chamber (37 °C, 5% CO_2) of the fluorescence microscope (Olympus IX81 inverted microscope). Nifedipine (Sigma-Aldrich) and lidocaine (Sigma-Aldrich) were reconstituted in dimethyl sulfoxide (DMSO, Sigma-Aldrich), according to the manufacturer's

protocol. The drugs were diluted in culture medium (I3M) to reach the final concentration ranging from 100 pM to 10 μM respectively. Prior to introducing the drug-containing medium, the force and calcium transients were recorded. An equivalent volume of media (without the drug) was added twice to the well of the 24-well plate. First, 500 μL of I3M medium was introduced and mixed with 1 mL of the medium within the well. Following a 15-min incubation period, contractility readouts and Ca^{2+} transients were observed using a fluorescence microscope at 4× magnification. Subsequently, 500 μL of the mixed medium was removed from the well, and another 500 μL of I3M medium was added for the second medium manipulation step. Force and calcium transient parameters were individually analyzed 15 min after each medium manipulation. Each drug concentration, ranging from 100 pM to 10 μM, was tested separately using the aforementioned medium addition strategy to attain the desired drug concentration within the medium of the well. After 15 min of the treatment of each concentration, the contractility readouts and Ca^{2+} transients were observed using a fluorescence microscope under the Texas red channel (λ_{ex} = 595 nm, λ_{em} = 615 nm) and FITC channel (λ_{ex} = 490 nm, λ_{em} = 525 nm), respectively, at 4X magnification. The ImageJ software (NIH) stack plugin was used to calculate the average fluorescence intensity of an area of nanocomposite microwires in the tissue. Contractility was calculated as described above. The videos for tracing calcium transients were analyzed using a custom-designed MATLAB algorithm as we described [27]. The ratio of peak fluorescence intensity to baseline intensity of tissues (dF/F_0) was calculated to measure the relative changes in intracellular Ca^{2+} in response to the drug compound. The force and calcium amplitude values for analyzing IC50 were normalized to the values of the force and calcium amplitude upon second media wash to account for any excitability in the tissue due to the shear force from media changes. IC50 value and 95% confidence interval were obtained by Prism 9.4.1.

Statistical analysis: Statistical analysis was performed using Prism 9.4.1. Differences between experimental groups were analyzed by one-way ANOVA (more than two groups), two-way ANOVA, or *t*-test (among two groups). The normality test (Shapiro-Wilk) was performed for one-way ANOVA and two-way ANOVA. Statistical significance was set at p < 0.05 and indicated in figures as * p < 0.05, **p < 0.01, ***p < 0.001, ****p < 0.0001.

3. Results

3.1. Establishment of an automated fabrication of multiwell heart-on-a-chip devices

We developed a simple and rapid fabrication approach for automated and scalable production of multiwell heart-on-a-chip platforms. To create the device in a high-throughput manner, a combination of hot embossing and 3D printing was implemented (Fig. 1A, Movie S1). A polystyrene plate with patterned microwells for tissue cultivation and with carbon electrodes was generated by hot embossing. In principle, hot embossing can result in microwells of any configuration (24-well,
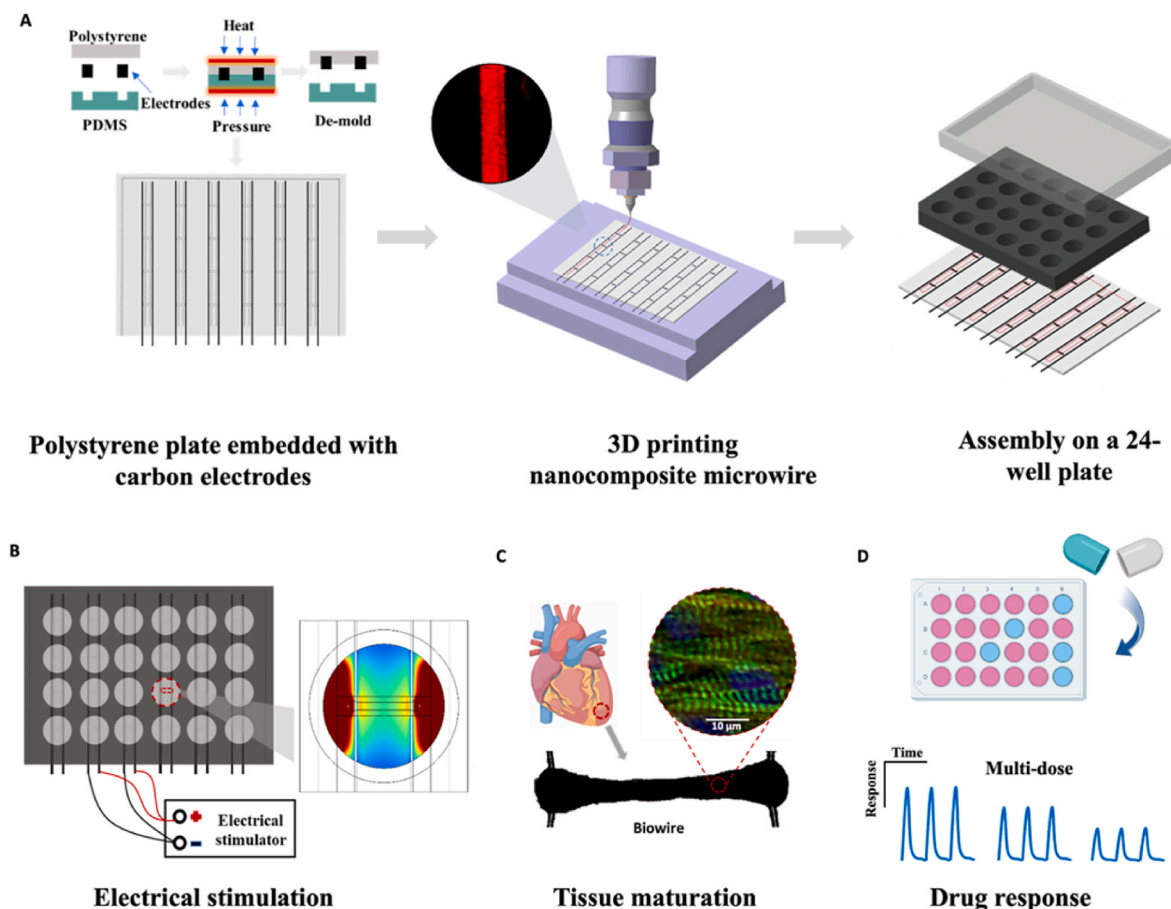
Fig. 1. Schematic illustration of the scalable fabrication of multiwell-plate devices for the cultivation of mature human Biowire II cardiac tissues. (A) Overview schematics of a 24-well plate device fabrication: hot-embossing of the base plate with embedded carbon electrodes in the 24-well format, 3D printing of TPE/QD microwires on the base to obtain a 24-well plate device by bonding a bottomless well plate and the electrode-embedded base. (B) Assembled 24-well plate device for the cultivation of cardiac tissues, allowing electrical stimulation. (C) The multi-well plate device with built-in electrodes for engineering anisotropic matured cardiac tissues which mimic native heart tissue. (D) The multi-well plate platform enabled non-invasive assessment of drug responses.

96-well, 384-well) patterned into the polystyrene sheet, with an example of a 24-well plate device illustrated (Fig. 1A). To provide anchor points for tissue formation, an array of soft elastic microwires were 3D printed using TPE/QD nanocomposite inks and directly deposited on both sides of each microwell on the base plate (Movie S2). The multiwell plate platform was finally generated by the thermal bonding of a bottomless well plate (e.g. 24-well) and the electrode-embedded base with flexible TPE/QD microwires. The incorporated carbon electrodes were used to stimulate tissues over several weeks to promote tissue maturation (Fig. 1B). The tissues, which wrapped around the parallel microwires in each microwell of a multiwell device, were expected to exhibit an anisotropic architecture. This architecture was characterized by a well-aligned sarcomere structure that recapitulates the native myocardial tissues due to the uniaxial tension provided by the TPE/QD microwires (Fig. 1C). The inclusion of carbon electrodes further allowed for rate control during drug testing, enabling the separation of chronotropic and inotropic drug effects (Fig. 1D). Additionally, the deflection of the nanocomposite wires was utilized to quantify the contractile dynamics (Fig. S1).

3.2. Finite element modelling of electric field distribution for effective device design

Increasing the number of tissues present on a single footprint of the multiwell plate (i.e. moving from 24- to 384-well plate) can significantly enhance the drug testing throughput. However, achieving effective tissue pacing for drug testing and maturation requires a uniform electrical field distribution within the well, which may impose a lower limit on the number of feasible tissues on a plate. Upon finite element modelling of electrical field distribution around the carbon electrodes within the well, as a function of well size, variations in the field distribution were noted between the standard setup (Biowire II strip in a 10 cm Petri dish) and multiwell models (Fig. 2A, Fig. S2). Specifically, a more homogeneous electric field distribution between the two electrodes was noted in the culture medium of the 10 cm Petri dish, compared to that of the multiwell models (Fig. 2B and C). In the well-plate models, smaller wells had higher electric field variation along the vertical plane of the hydrogel approximating the tissue (Fig. 2C, top row) and a lower homogeneity of electrical field distribution along the horizontal plane of the hydrogel approximating the tissue (Fig. 2C, bottom row). Fig. 2D shows the line profile of the electric field (V/m) along the axial direction of the hydrogel approximating the tissue in the center plane. When an electric field was applied, the field magnitude near the walls of the microwires in all models was significantly higher than the average value. Yet importantly, in the 24- and 96-well configuration, the field was relatively constant along most of the length in the cross-section of the tissue culture microwell (Fig. 2D). The electrical field distribution in the culture medium and hydrogel approximating the tissue in the multiwell model was not affected by the material used for the microwires when standard elastomer wires (POMaC) were compared to the new TPE wires (Fig. S3). In these models, standard dielectric properties of the constituent materials were used (Table S1). Overall, due to the enhanced field distribution in the 24-well and the 96-well configuration, over the 384-well configuration, the fabrication of 24- and 96-wells was pursued further.

3.3. Automated multiwell device production increases efficiency over manual fabrication of biowire II setup

A combination of hot embossing and 3D printing techniques (Fig. 3A) was used to fabricate the multiwell plate device (Movie S1), eliminating the need for manual manipulation and insertion steps that require a highly skilled and dexterous operator (Movie S3). The process enabled the formation of both 24-well (Fig. 3B–D) and 96-well plate devices (Fig. 3E–G) with uniform TPE/QD microwires and paralleled carbon electrodes in each well. A detailed comparison of fabrication steps between a standard Biowire II platform versus the multiwell plate

devices (Fig. 3A), demonstrates a significant difference in the fabrication time at each step (Fig. 3H). A dramatic decrease in fabrication time per platform from 3890 min (Biowire II setup) to 70 min (24-well plate) and 74 min (96-well plate) was achieved by this automated production process (Fig. 3I). When time per tissue well is considered, a decreased production time from 483 min (Biowire II) to 2.9 min (24-well) and only 0.77 min (96-well) is achieved (Fig. 3J). We estimated the labor and material cost per well for device production, to be approximately \$4.8/well for a 24-well format and \$2.7/well for a 96-well format, while the cost per well in Biowire II is approximately \$13.9/well. The automated approach which requires the use of 3D printers for TPE/QD wire deposition may require a significant infrastructure investment that has not been factored into the calculation when compared to the manual production of Biowire II wells. Through this new fabrication process, our previous Biowire II platform fabricated via an entirely manual process is scaled up from an 8-microwell chip to a patterned 24-well or 96-well plate, thus speeding up the platform production per microwell by 17,500 % in a 24-well plate and 69,000 % in a 96-well plate compared to Biowire II platform (Fig. 3K).

3.4. Characterization of nanocomposite microwires

To detect the contraction behaviour of cardiac tissue from the deflection of the elastic microwires, styrene-ethylene/butylene–styrene (SEBS) block copolymer, ie thermoplastic elastomer, was rendered fluorescent by core-shell CdSe/ZnS quantum dots (QDs) (Fig. 4A and B). We customized the nanocomposite inks and printed them into microwires (diameter of 60 ± 4 μm) with different resolvable colors that can be excited using different excitation wavelengths (fluorescence λ_{em} 450 nm and λ_{em} 630 nm) (Fig. 4A and B). The TPE/QD nanocomposite presented no degradation after immersion of nanocomposite films in culture media for up to one month (Fig. 4C), demonstrating suitable stability for the long-term cell culture. The bending properties of elastic nanocomposite microwires (100 μm diameter) were assessed by placing the customized micromechanical tester probes at the center of the TPE/QD microwires followed by microwire displacement (Fig. S1A). QDs in the nanocomposite microwires unaltered the bending properties (Fig. 4D and E) and stiffness of the microwire (Fig. 4F), showing similar force-displacement curves to those of TPE microwires. Through this property, the nanocomposite microwires in the multiwell plate device are used as force sensors to monitor the contractile behavior of the cardiac tissues (Fig. S1). Young's modulus of TPE/QD was significantly higher than that of POMAC, however, both values are similar to the native heart elasticity (Fig. S4). Also, we provide additional data (Fig. S5) to further demonstrate the difference in swelling ability. POMaC polymer wires were compared to TPE/QD wires, upon swelling in distilled water, PBS and culture media for 24hrs. The swelling as indicated by the diameter increase in water was significantly higher with POMaC compared to TPE in water, which could prove detrimental in some instances, ie in the presence of highly hydrophilic molecules, yet it was comparable in PBS and culture media.

3.5. Maturation of hiPSC derived cardiac tissues

Due to the generally improved electrical field distribution (Fig. 2), we focused our maturation studies on the 24-well plate device with 60 μm, microwires that are similar to the mechanical properties of native cardiac muscle as we demonstrated [42]. The new platform cytocompatibility was first validated with neonatal rat cardiac tissues. The majority of cells remained viable in cardiac tissues generated from neonatal rat cardiomyocytes after two weeks of tissue culture using the multiwell plate device (Fig. S6). The viability staining was consistent with that in tissues generated in the standard Biowire II setup incorporating POMaC wires (Fig. S6), suggesting overall device biocompatibility, thus motivating the cultivation of human tissues in the next step.

A mixture consisting of hiPSC-derived cardiomyocytes and primary
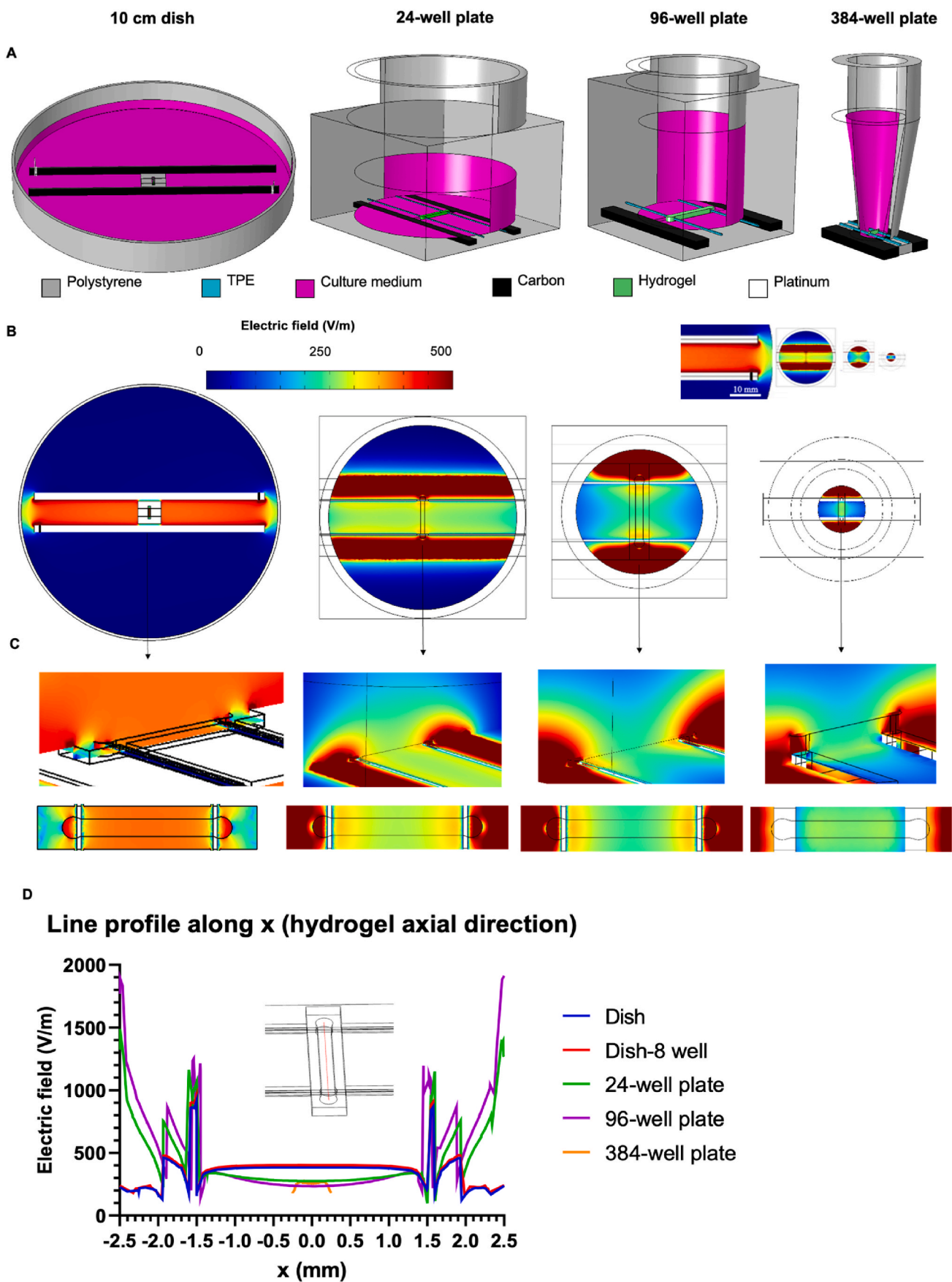
Fig. 2. Electrical field distribution in Biowire II cultivation setup and multi-well plate devices. (A) Schematic illustration of the cultivation setup. The standard setup consists of a 10 cm Petri dish with an 8-well polystyrene strip. The high throughput setup consists of a multi-well plate configuration, with one tissue per well. The tissue is applied into the microwell for cell seeding. Cardiac tissue is approximated by a hydrogel for mathematical modelling purposes. Two parallel anchor wires are constructed from POMAC in the standard 10 cm Petri dish setup and TPE/QD nanocomposite wires in a high-throughput setup. Carbon electrodes are included for electrical stimulation and culture media is applied. (B) 2D view of the electrical field distribution in different models. (C) Zoomed-in 2D view of the electrical field distribution in culture media around the hydrogel, approximating the tissue. Note: Hydrogel in the 384-well plate device is 5 times smaller laterally with the same thickness compared to those in the other models. (D) Line profile of electric field (V/m) along the axial direction of the hydrogel approximating the tissue in the microwell. * Due to the small size of the well of 384-well, the TPE/QD wire in 384-well plate is not annotated here.

cardiac fibroblasts was seeded in each microwell of the 24-well plate device using a hydrogel and was reorganized to generate 3D cardiac tissues that are physically attached to the nanocomposite microwires (Movie S4). The multi-well platform enabled higher yield of hiPSC-CMs-based 3D cardiac tissues, with a high consistency of tissue formation (Fig. 5A). The tissues underwent notable cell-gel compaction during the first week after seeding until the diameter eventually stabilized (Fig. 5B and C).

To demonstrate the capability of the multiwell plate device for a long-term culture of mature cardiac tissues, the cardiac tissue in a 24-well plate device was exposed to an electrical field stimulation starting from 7 days after cell seeding (Fig. S7), the initial time period required for tissue remodeling due to cell-gel compaction (Fig. 5B and C). We used a previously established protocol [5] of weekly frequency increase to implement tissue maturation (Fig. S7). Electrical excitability parameters improved with maturation, as manifested by the decreasing excitation threshold (ET) and a significant increase in the maximum capture rate (MCR), upon electrical stimulation (Fig. 5D and E).

In situ recording of the nanocomposite microwire displacement provides a non-invasive readout of the contractile dynamics of engineered cardiac tissue, such as active force, pre-tension, and peak duration (Fig. 5F–J, Fig. S1, Movie S5). In each microwell, the nanocomposite microwire bent upon myocardial tissue contraction, with displacement that is directly related to tissue contractile forces (Movie S5). Through recording the bending movement of the fluorescent microwire, wire deformation can be converted into contractile force, using previously generated calibration curves (Fig. S1, Fig. 4E).

Before electrical stimulation, the tissues (at week 1) presented a relatively flat force-frequency relationship (FFR), without post-rest potentiation (PRP) of force (Fig. 5F). By contrast, after 4-week stimulation (at week 5 of culture), they exhibited a positive FFR profile and PRP of force. The active force was profoundly increased (Fig. 5G), and passive tension was significantly decreased (Fig. 5H) in the tissues at the end of cultivation with electrical stimulation maturation protocol. When paced at 3 Hz, the tissues subjected to the maturation protocol (5 weeks of culture) were successfully captured in contrast to the initial tissues (1 week of culture) (Fig. 5F). The contraction and relaxation times shortened significantly after 5 weeks of culture, in comparison to the initial tissues (week 1), as expected based on the improved capture rate (Fig. 5I). After pacing at 3 Hz, the PRP of tissue force (week 5) at 1 Hz pacing was significantly higher (4 times) than the value for the tissues before electrical conditioning (Fig. 5J). Additionally, the cardiac tissue displayed longitudinal sarcomeric alignment of contractile proteins after 5 weeks in tissue culture with electrical stimulation for maturation (Fig. 5k). Importantly, we also demonstrated the capability to cultivate human iPSC-derived cardiac tissues in the 96-well plate device (Fig. S8). Taken together, these observations suggest that long-term electrical conditioning elicited tissue maturation in the 24-well plate device, fabricated by an automated process that eliminated the most challenging manual fabrication step, specifically the microwire insertion.

3.6. Drug testing in the multiwell platform with nanocomposite microwires

To demonstrate the application of the device, tissue responses to increasing doses of nifedipine, an L-type Ca^{2+} channel blocker, and lidocaine, a blocker of voltage-gated sodium channels, were evaluated (Fig. 6). The drug responses of cardiac tissues under electrical

stimulation can be demonstrated by tracing the force and calcium transient of cardiac tissues in our platform (Fig. 6A). Nifedipine exposure led to a dose-dependent decrease in both force and Ca^{2+} transients in the cardiac tissues (Fig. 6B, Movie S6).

The half-maximal inhibitory concentration (IC50) of nifedipine was 3.6 nM (95% confidence interval (CI) of 0.8–14.9 nM) for contractile force and 0.8 nM (95% CI of 0.3–2.6 nM) for Ca^{2+} transients (Fig. 6C), in agreement with values from previous studies (6 nM–60 nM) [43–46]. Similarly, the application of the sodium channel blocker lidocaine led to a dose-dependent decrease in the contraction force (Fig. 6D). IC50 of lidocaine was 0.2 μM (95% CI of 0.03–1.9 μM) for force and 0.1 μM (95% CI of 0.02–0.9 μM) for calcium transients (Fig. 6E). These results demonstrate that lidocaine's inhibitory effects are of similar magnitude as compared to the values in the literature [45,47–49]. Overall, these results validate the utility of the new multiwell plate device with nanocomposite microwires and carbon electrodes in drug testing.

4. Discussion

Recent advances describe the development of sophisticated cardiac tissue models [50–54] and the ability for *in situ* functional assessments [5,17–20]. Challenges remain in refining the physiological relevance and scalability of these sophisticated cardiac tissue models while also enabling non-invasive *in situ* contractile assessment and driving an anisotropic cell orientation.

Currently, contractile behavior including beating rate and maximum force, are routinely evaluated by optical analysis (e.g., direct optical imaging [55], fluorescent [56], laser-based sensing [57]) or electrical (e. g., strain and impedance [58]) sensors. A precise assessment of contractile dynamics of trabecula-like cardiac tissues can be achieved through either the deflection of PDMS posts [8] or the movements of PDMS cantilevers [59] and thin films [60,61]. However, the utilization of PDMS may lead to indiscriminate absorption of small molecules, thereby influencing cellular activity and constraining the device's potential applications [62]. This motivates the development of plastic and polymer such as SEBS [63] structures that decrease small molecule absorption [64].

However, the current Biowire II platform, along with many other organ-on-a-chip devices, is presently fabricated manually, resulting in low throughput. This manual approach may be inadequate in meeting the increasing industry demands and requires a highly skilled and dexterous operator (Movie S2). Limited automation in the production and cultivation workflows ultimately limits the adoption of organ-on-a-chip and microphysiological systems. Through the automated fabrication process described here, the Biowire II platform can be scaled up from an 8-microwell chip to a patterned 24-well or 96-well plate, increasing the number of tissues that can be grown in each device, all the while eliminating the need for a skilled fabrication operator and enhancing fabrication efficiency by 17,5000–69,000% per well. Also, the wire deposition success rate in the microwell was approximately 60% when using the manual deposition in Biowire II. However, this rate significantly increased to approximately 90% when utilizing the multi-well plate device with this new approach. The scale-up was achieved by the integration of three classes of materials via multi-material automated processing: a polystyrene base, carbon electrodes and TPE/QD nanocomposite wires within a footprint of 127×85 mm^2, equivalent to the dimensions of the multiwell plate. It is important to note that the
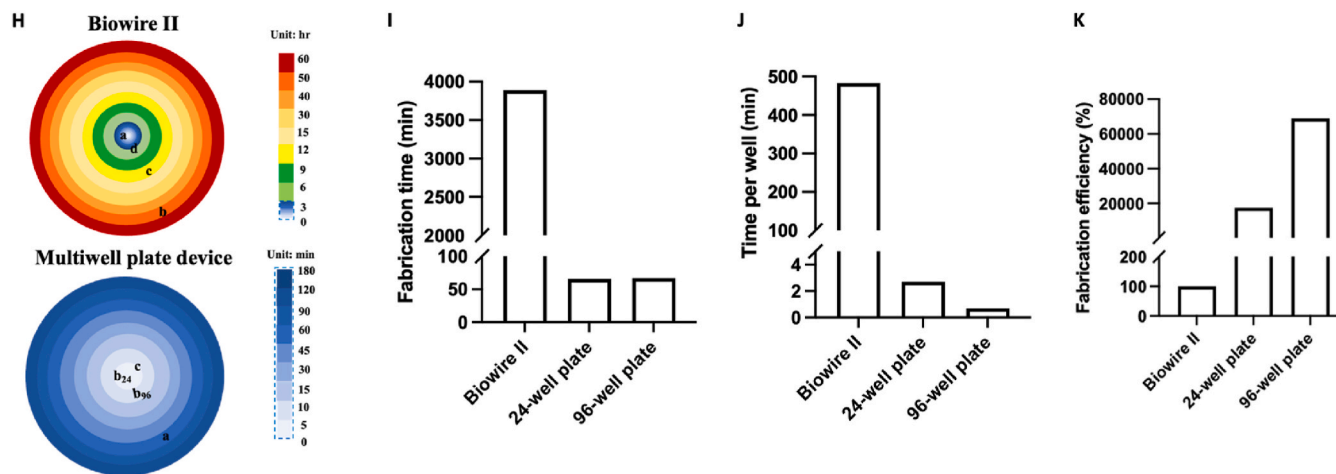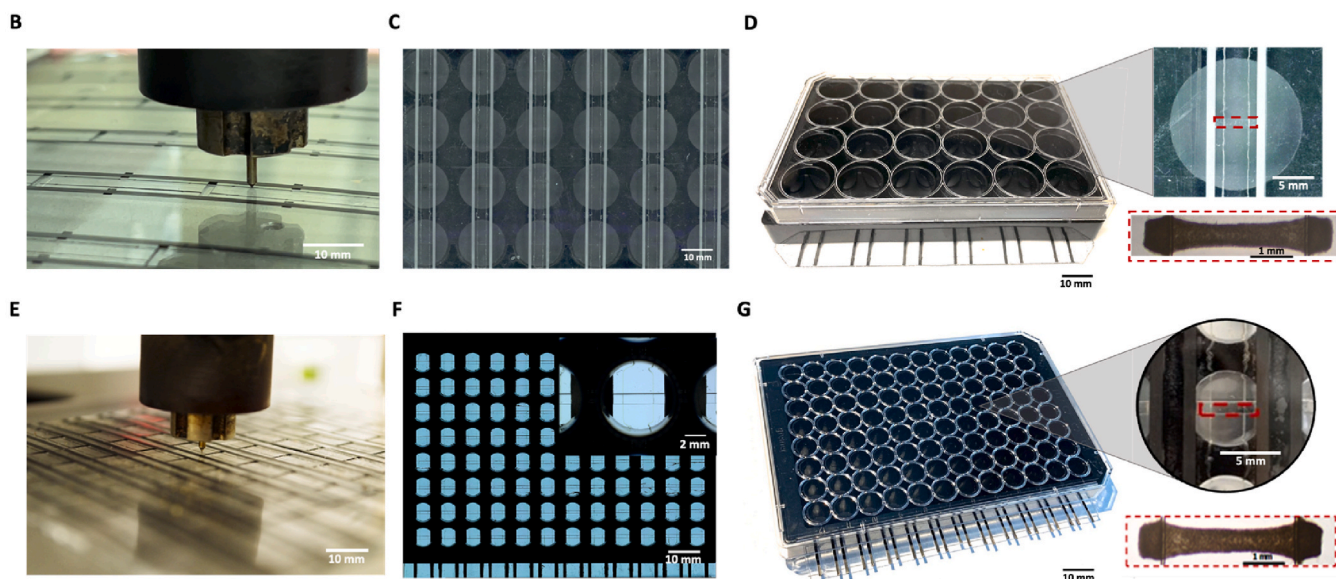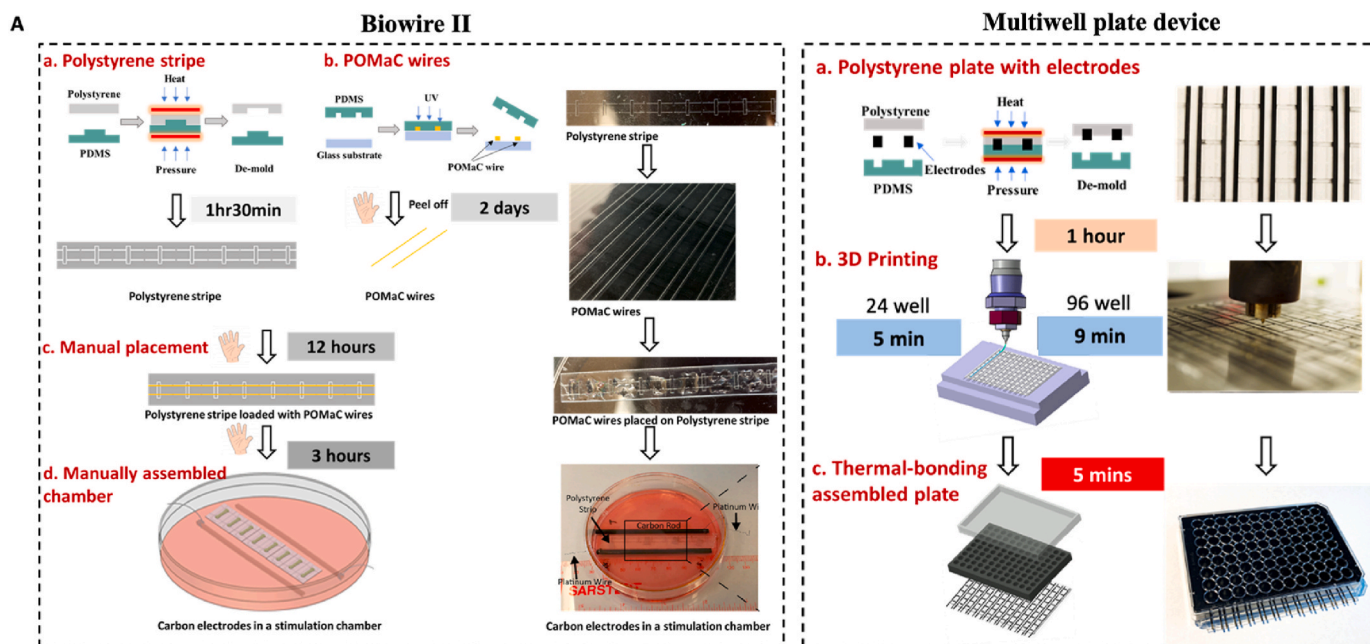
(caption on next page)

Fig. 3. Automated fabrication of 24- and 96-well plate heart-on-a-chip devices (A) Workflow comparison for the manual production of Biowire II platform and automated production of 24-well and 96-well devices. Biowire II platform fabrication consists of a) manual cutting of a polystyrene strip from a hot-embossed base plate, b) molding of POMaC microwires, c) manual placement of POMaC microwires on the polystyrene strip and d) manual assembly of a carbon electrode and of the polystyrene microwell strip in a Petri dish. Multiwell plate device fabrication involves a) hot-embossing of a polystyrene plate with carbon electrodes, b) 3D printing of TPE/QD nanocomposite microwires on the polystyrene plate and c) thermal-bonding of a bottomless plate to a multiwell plate device. (B) 3D printing of nanocomposite microwires on carbon electrode-embedded 24-well base. Scale bar: 10 mm. (C) Keyence digital microscopy of a 24-well plate device, prepared by the automated production process. Scale bar: 10 mm. (D) A digital camera image of a 24-well plate device. Scale bar: 10 mm. The inserted image shows the magnified image of one well that consists of a microwell, nanocomposite wires and electrodes and the microwell is labelled in a red frame for tissue formation. Scale bar: 5 mm. A cardiac microtissue, generated from a 24-well plate device, was presented in a microwell labelled in a red frame. Scale bar: 1 mm. (E) A digital camera image of 3D printing of the nanocomposite patterns on the electrode-embedded 96-well base. Scale bar: 10 mm. (F) Keyence digital microscopy of a 96-well plate device. Scale bar: 10 mm. The inserted image shows the magnified view of one well consisting of a microwell, nanocomposite wires and electrodes in the plate, scale bar: 2 mm. (G) A digital camera image of a 96-well plate device. Scale bar: 10 mm. The inserted optical image shows the magnified of one well and the microwell in the well is lablled in a red frame. A cardiac microtissue, generated from a 96-well plate device, was presented in a microwell labelled in a red frame. Scale bar: 1 mm. (H) The heat maps summarize the estimated time used for each step to fabricate Biowire II (top) and multiwell plate device (bottom). Letters a, b, c, d correspond to the time steps indicated in part A. The scale bar (top) presents the time scale required for each step of Biowire II fabrication, unit: hour (hr). The scale bar (bottom) shows the time scale required for each step of multiwell plate device, unit: minute (min). The comparison of I) the total fabrication time of a device, J) the fabrication time per well in each device and K) the increase in the fabrication efficiency (%) among Biowire II setup, 24-well plate and 96-well plate.
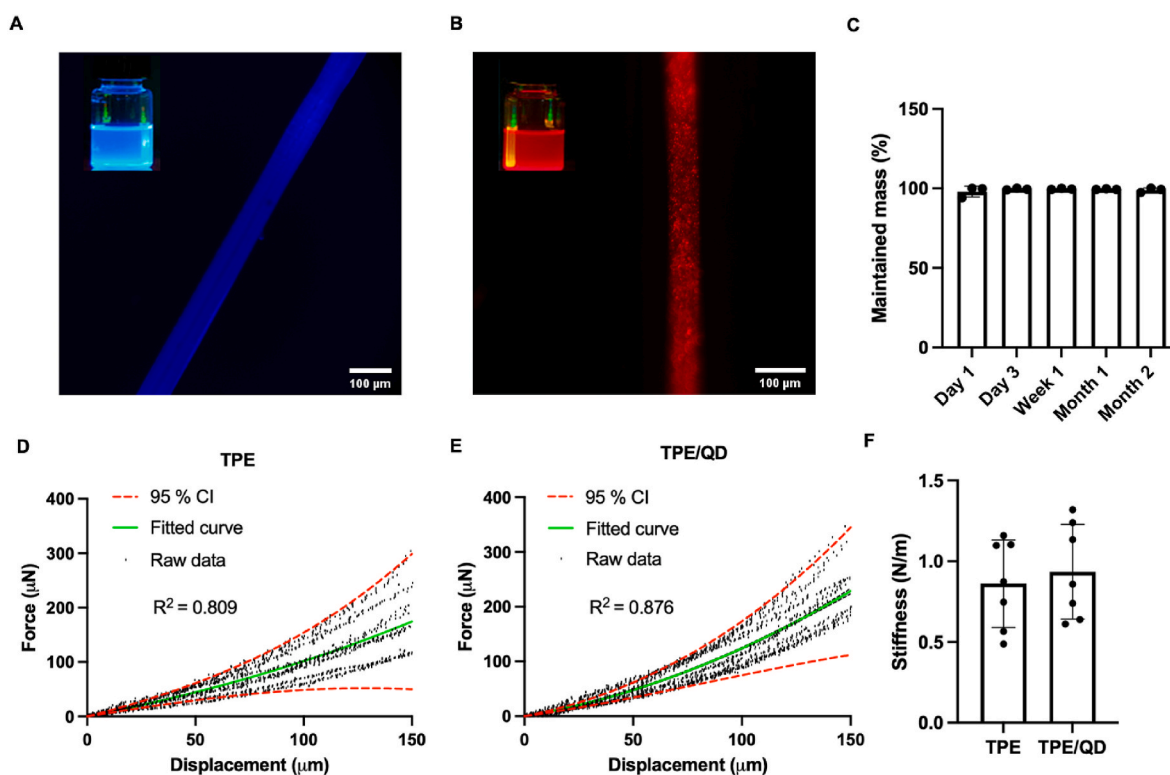

Fig. 4. Characterization of nanocomposite microwires used as tissue anchor points and displacement sensors in multi-well plate devices. Fluorescence microscopy images of the nanocomposite wire doped with CdSe/ZnS core-shell type QD nanoparticles with different fluorescence λ_{em} A) 450 nm and B) 630 nm, respectively. Scale bar: 100 μm. Inserts demonstrate the fluorescence of QDs in toluene. (C) Maintained mass (%) of nanocomposite film after immersion in culture medium for 24 h, 3 days, 1 week, and 1 month, at room temperature. n = 3, data shown as average ± s.d. Force-displacement curves of D) TPE microwires and E) TPE/QD nanocomposite microwires, with a diameter of 100 μm. The fitted curve and R^2 values were presented and analyzed by Prism 9.0, n ≥ 7. (F) The stiffness of TPE and TPE/QD microwires was calculated from the force-displacement curves of both microwires. (n = 7, data shown as average ± s.d.).

TPE/QD wires and polystyrene base were both made from thermoplastic materials, ensuring effective thermal bonding between the wires and the base, and thus preventing any unintended wire movement out of the base during tissue contraction. The wires in the microwell of the base plate could move freely, accurately sensing tissue forces.

Previously, we also described the fabrication of 96-well plates with POMaC wires, that were generated through a slow process of wire casting in PDMS stamps [65]. In comparison to POMaC polymer microwires, the use of QDs and thermoplastic elastomers allows for the customization of the microwire color. We anticipate that it would be possible to further modify POMAC with QDs, by incorporation of QDs into the pre-polymer liquid before the final step of photocrosslinking. QDs that are modified and stabilized with e.g. –COOH groups to afford

some hydrophilicity would likely be most useful. Here, we used QDs with hydrophobic surface modifications (stabilized with octadecylamine ligands) to match the hydrophobic nature of TPE. Additionally, POMAC could be further modified with amino acids to modulate its intrinsic fluorescence [66–68]. For example, Yang's lab developed "one-pot" reaction to synthesize citrate-based biodegradable photoluminescent polymers (BPLPs) [66]. The fluorescence of BPLPs emanated from a conjugated ring formed from citrate and L-cysteine.

The tissue maturation was not successfully achieved in our previously customized multiwell plate [20] (96 well format) but was achieved in our multiwell plate device here (24 well format). This was most likely due to a more uniform electrical field distribution in a 24-well plate device compared with other multiwell models as demonstrated
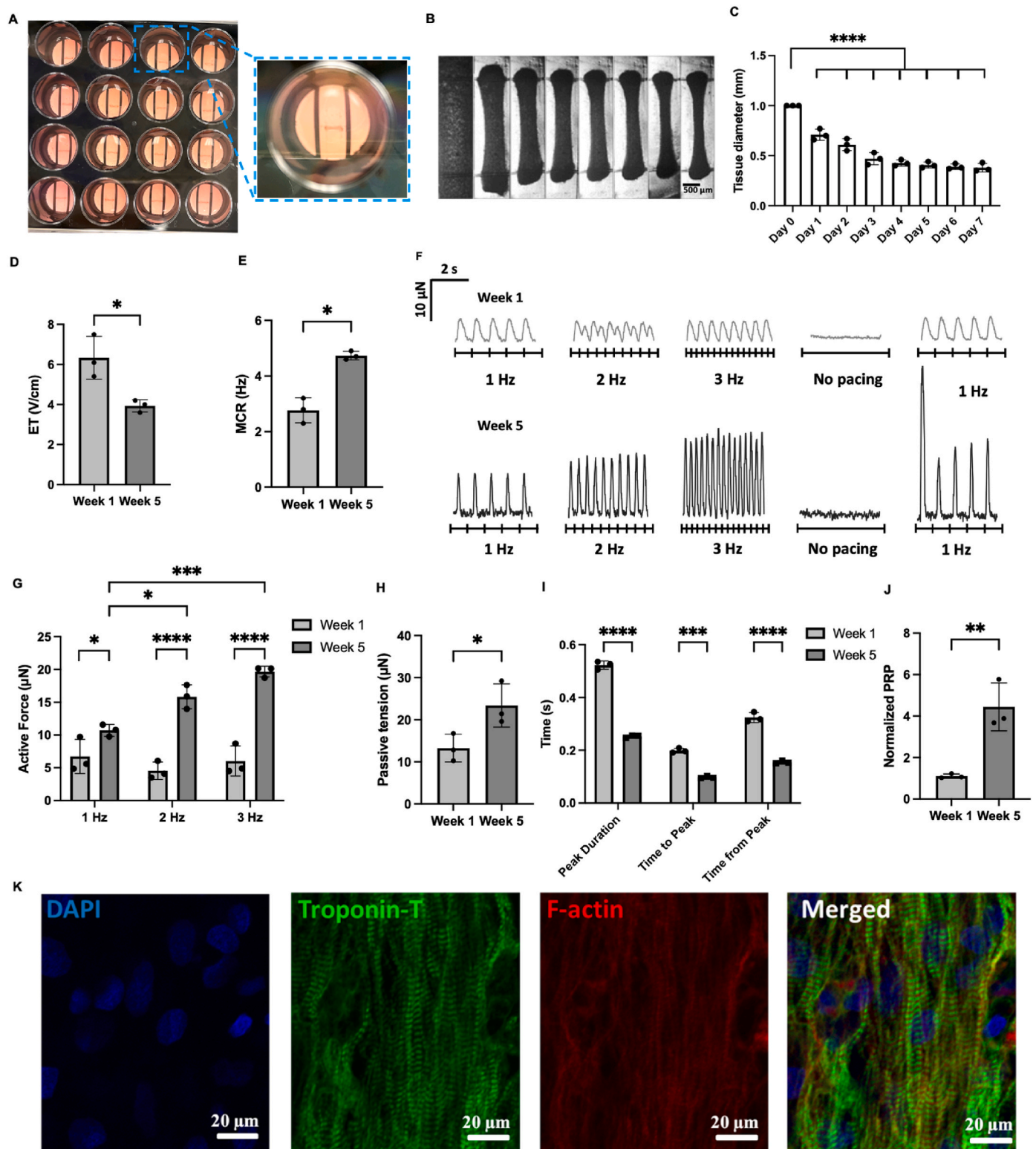
Fig. 5. Assembly and function of hiPSC-based cardiac tissues in the 24-well plate device. (A) Cardiac microtissues are generated in the 24-well plate device, with the insert showing the tissue in one well. (B) Representative tissue images captured on days 0–7 after cell seeding, and C) the change in tissue diameter over the 7 days. (n = 3, one-way ANOVA analysis, ****p < 0.0001, data are shown as average ± s.d.) D) Excitation threshold (ET) and E) maximum capture rate (MCR) of cardiac tissues over 5 weeks in culture (n = 3). (F) Representative force traces of cardiac tissues after 1 week and 5 weeks (4 weeks of electrical stimulation) of cell culture, separately, and under different frequency rates (1–3 Hz). Quantification of G) active force under pacing from 1 Hz to 3 Hz, H) passive tension under electrical stimulation at 1 Hz, I) peak duration, time to peak and time from the peak of the tissues paced at 3 Hz and J) PRP values normalized to the average value of the active force of the tissues paced at 1 Hz (the first pacing frequency of force traces in Fig. 5F), between week 1 and week 5 of tissue culture. (n = 3, *t*-test or two-way or ANOVA analysis, *p < 0.05, **p < 0.01, ***p < 0.001, ****p < 0.0001, data are shown as average ± s.d.) (K) Confocal images of representative cardiac tissue after 4-week stimulation in the platform, immunostained for nucleus (DAPI), cardiac troponin-T (green) and sarcomeric F-actinin (red) (n = 3).
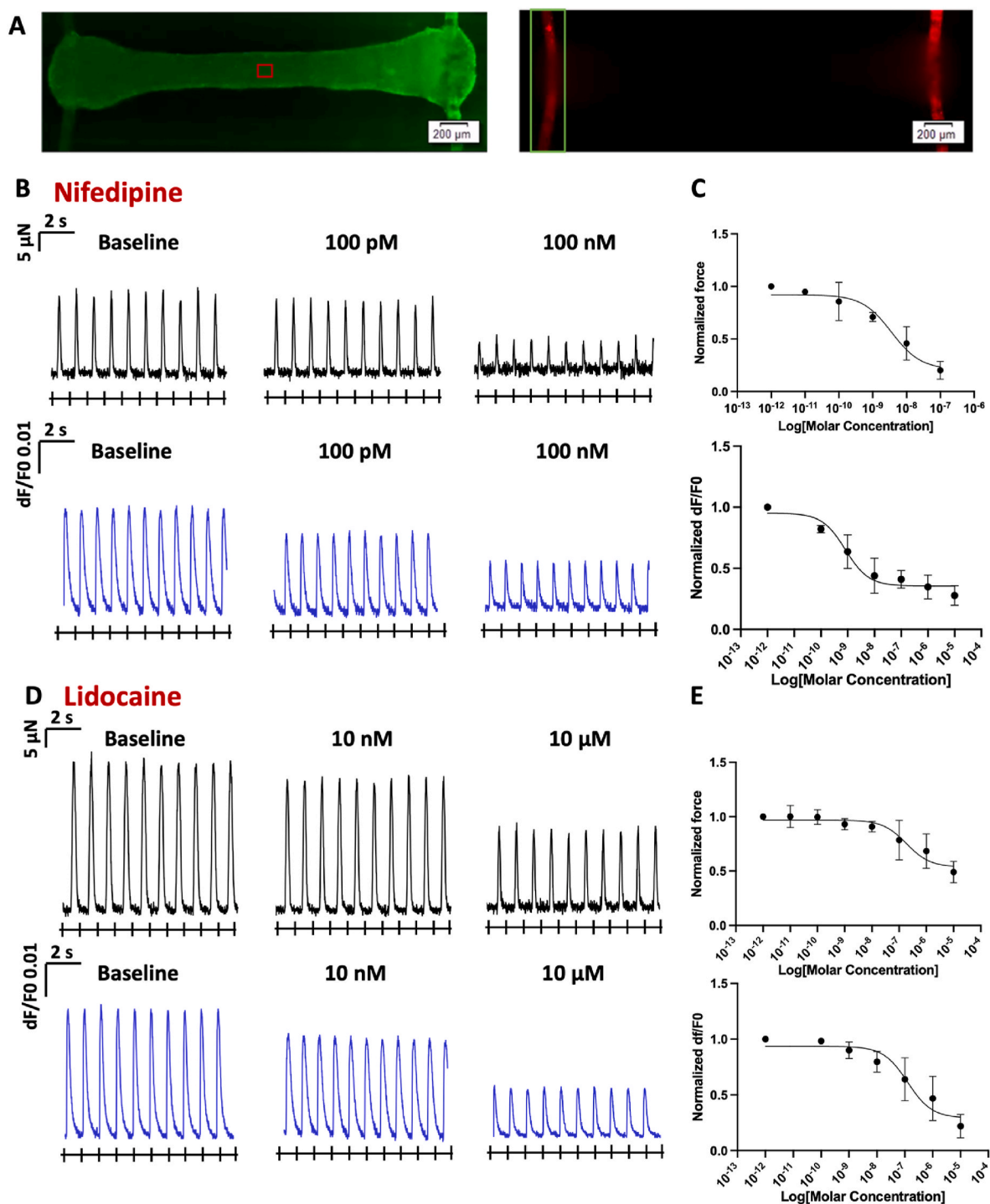
Fig. 6. 24-well plate device enables *in situ* **recording of contractile force and calcium transients in drug-exposed cardiac tissue.** A) Fluorescent signals of a cardiac tissue loaded with a Ca^{2+} Fluo-4 dye and the nanocomposite microwires bending by tissue contraction, scale bar 200 μm. B) Typical force (black) and Ca^{2+} transients (blue) of cardiac tissues before drug treatment (baseline) and treated with nifedipine at concentrations of 100 pM and 100 nM. (C) Drug dose-response with normalized force and Ca^{2+} transients amplitude (dF/F0) for tissues treated with nifedipine. D) Typical contractile force (black) and Ca^{2+} transients (blue) of cardiac tissues before (baseline) and after treatment with lidocaine at concentrations of 10 nM and 10 μM. E) Drug dose-response with normalized force and Ca^{2+} transients amplitude (dF/F0) of cardiac tissues treated with and E) lidocaine. The normalized values are normalized with respect to the baseline of each individual tissue. (n = 3, data are shown as average ± s.d.).

by mathematical modeling. POMaC is inherently biodegradable whereas TPE is not. Yet, since most experiments last weeks, the stability of POMaC is sufficient for this application as well, since appreciable degradation would require a period of months [5,69]. Additionally, our recent report demonstrates the TPE/QD microwires incorporated on top of a multi-electrode array for single tissue generation [69]. In

comparison to that previous work, we had to optimize the 3D printing process to enable uniform wire deposition over a large 127 × 85 mm² area.

The majority of organ-on-a-chip devices are currently made from PDMS, a material known for its availability, affordability, and compatibility with soft lithography - a widely used fabrication technique. Yet, it

suffers a range of limitations, one of which is drug absorption. There is a critical need for advancements in biomaterial science to develop new materials suitable for manufacturing organ-on-a-chip devices [28]. One promising biomaterial introduced here is QD-doped TPE. Importantly, the advances in biomaterial science and engineering will also enable multi-material processing approaches that are needed to fabricate devices amenable to high-throughput fabrication, while at the same time incorporating mechanical properties of a substrate that are similar to the tissue being modelled and exhibiting general biocompatibility.

Even though our platform did not feature any patterns or structures for directly guiding cell alignment, the electrical conditioning and tension imposed by the remodeling matrix anchored at the two ends [42], induced uniform longitudinal alignment of sarcomeric contractile proteins in the cardiac tissue. Although we optimized the device for the cardiac tissue and to support tissue maturation from hiPSC-derived CMs, the physical features and electrical stimulation parameters of the device could be easily tuned in the future to generate tissues from other cell types, such as skeletal muscle cells and modeling genetic disease from patient-derived cells. From our observation, the cardiac tissue does not adhere to the carbon wires (i.e. carbon electrodes). The tissue gets wrapped around the TPE/QD micowires. This occurs by the spontaneous process of cell-gel compaction. After fabrication, the entire plate (wires included) is treated with pluronic acid. Cardiac cells are then uniformly seeded into the microwell. Since they cannot attach to the bottom of the plate due to pluronic acid treatment, the cells start remodeling the gel due to their own tractional forces, a well-known process termed gel compaction. As the gel compacts, the tissue condenses in the middle of the well wrapping around the two TPE/QD wires. Thus, making the plate non-adhesive through pluronic acid treatment ensures a reproducible gel compaction process. Additionally, we used the gel volume (2.5 µl) and the cell concentration (6×10^7 cells/mL) that were optimized in our previous studies using Biowire II wells of identical geometry [70]. Previously, using mathematical modelling we have studied the remodeling of a tissue affixed to two anchor points and demonstrated the contribution of the cells' own tractional forces to creating a uniform tissue in a similar setting [71]. In rare instances when the tissues attach to areas outside the well and including carbon electrodes, a gentle prodding by a pipette tip or tweezers ensures that the tissue detaches from the base and assumes a position in the well wrapping around the TPE/QD wires.

It is important to note that the tissue does not really actively attach to the wires, primarily due to pluronic acid treatment. Instead, it wraps around the wires due to the process of gel compaction. This ensures that tissues in different wells have a comparable adhesion strength. Given that the tissue wraps around the wires, and this wrapping may result in different tissue diameters on the wires, we employed customized probes to recapitulate the tissue diameter and curvature on the wires. These probes were essential for generating accurate force-displacement calibration curves. Subsequently, we calculated the contraction force of the tissue by interpolating the calibration curves based on measurements of tissue widths on the nanocomposite wires and the average tissue width between two wires. As with any emerging technology, the described heart-on-a-chip well plates have room for development. Despite electrical stimulation improving tissue maturation in the 24-well format, more stimulation protocols may be required for more robust maturation. In addition, the current investigation focused on the formation of cardiac tissue from hiPSC-CMs and fibroblasts. Future research could investigate the use of other cell types, such as iPSC-derived cardiac progenitor cells, endothelial or epicardial cells, to generate more intricate cardiac tissue constructs. Incorporating additional physiological characteristics into heart-on-a-chip models is another potential avenue for future research. For instance, the incorporation of mechanical loading or shear stress could more accurately simulate the microenvironment of cardiac tissues in vivo and promote tissue maturation. Lastly, while the device format demonstrated in this study offers significant benefits, the electrical field distribution within the device could be optimized further. Additional computational modelling could identify more optimal electrode and well configurations for homogenous electrical field distribution throughout a tissue sample. For generating the tissues in the device, automatic cell dispensers extensively used in the pharmaceutical industry should be employed or automatic tissue generation by hydrostatic pressure [23,72] can be used and adapted for automated cell seeding in our multiwell plate device. The automation of wire-deflection readouts should be achieved further, ideally coupled with high-content imaging systems. Ultimately, the engineered human left ventricle [73,74], and a 3D bioprinted ventricle model [75] may replace trabeculae-like structures in drug development and disease modelling, due to their conceptual ability to predict ventricle dilatation and remodeling, as well as the ability to capture clinically relevant parameters such as ejection fraction [76].

5. Conclusions

The development of high-throughput, reliable, and reproducible heart-on-a-chip models is a rapidly evolving field with significant potential for applications in drug discovery and disease modelling. Using a combination of hot embossing and 3D printing of quantum dot/thermoplastic elastomer nanocomposite, the results of this study demonstrate the automated fabrication of a multiwell plate device format that enables high throughput device fabrication and eliminates the need for a dexterous operator. This format is superior to the existent Biowire II devices in terms of scalability, compatibility with standard liquid handling and imaging equipment, and the capacity to simultaneously cultivate multiple tissue samples. This automated method surmounts the difficulty of fabricating high-throughput devices with inert materials and the dimensions of a multiwell plate and enables the cultivation of mature cardiac tissues as a result of uniform electric field distribution in each well of the device. The versatility of 3D printing in precise deposition of TPE-based anchor points, may allow for the potential creation of other well-plate format devices for various tissues, providing a platform for high-throughput screening of drug candidates and disease modeling across different organ systems.

Ethics approval and consent to participate

Our study did not conclude any clinical study, animal experiments and human subjects.

Conflict of interest declaration

MR and YZ are inventors on an issued US patent that describes Biowire technology, which is licensed to Valo Health. They receive royalty income for this invention. Additionally, QW, YZ and MR are inventors of patent applications describing TPE/QD nanocomposite material and its 3D printing.

CRediT authorship contribution statement

Qinghua Wu: Conceptualization, Data curation, Formal analysis, Writing – original draft, Writing – review & editing. **Ruikang Xue:** Data curation, Formal analysis, Methodology, Writing – review & editing. **Yimu Zhao:** Formal analysis, Writing – original draft, Writing – review & editing. **Kaitlyn Ramsay:** Writing – original draft. **Erika Yan Wang:** Data curation, Visualization, Writing – review & editing. **Houman Savoji:** Conceptualization, Writing – review & editing. **Teodor Veres:** Conceptualization, Methodology, Writing – review & editing, Funding acquisition. **Sarah H. Cartmell:** Supervision, Writing – review & editing. **Milica Radisic:** Conceptualization, Funding acquisition, Methodology, Project administration, Resources, Supervision, Writing – original draft, Writing – review & editing.

Acknowledgements

Appendix A. Supplementary data

Supplementary data to this article can be found online at https://doi.org/10.1016/j.bioactmat.2023.10.019.

References

[1] S.M. Paul, D.S. Mytelka, C.T. Dunwiddie, C.C. Persinger, B.H. Munos, S.R. Lindborg, A.L. Schacht, How to improve R&D productivity: the pharmaceutical industry's grand challenge, Nat. Rev. Drug Discov. 9 (3) (2010) 203–214.

[2] J. Wang, C. Wang, N. Xu, Z.-F. Liu, D.-W. Pang, Z.-L. Zhang, A virus-induced kidney disease model based on organ-on-a-chip: pathogenesis exploration of virus-related renal dysfunctions, Biomaterials (2019), 119367.

[3] Y. Wang, L. Wang, Y. Zhu, J. Qin, Human brain organoid-on-a-chip to model prenatal nicotine exposure, Lab Chip 18 (6) (2018) 851–860.

[4] I. Maschmeyer, A.K. Lorenz, K. Schimek, T. Hasenberg, A.P. Ramme, J. Hübner, M. Lindner, C. Drewell, S. Bauer, A. Thomas, A four-organ-chip for interconnected long-term co-culture of human intestine, liver, skin and kidney equivalents, Lab Chip 15 (12) (2015) 2688–2699.

[5] Y. Zhao, N. Rafatian, N.T. Feric, B.J. Cox, R. Aschar-Sobbi, E.Y. Wang, P. Aggarwal, B. Zhang, G. Conant, K. Ronaldson-Bouchard, A platform for generation of chamber-specific cardiac tissues and disease modeling, Cell 176 (4) (2019) 913–927, e18.

[6] P. Vulto, J. Joore, Adoption of organ-on-chip platforms by the pharmaceutical industry, Nat. Rev. Drug Discov. 20 (12) (2021) 961–962.

[7] K. Ronaldson-Bouchard, G. Vunjak-Novakovic, Organs-on-a-chip: a fast track for engineered human tissues in drug development, Cell Stem Cell 22 (3) (2018) 310–324.

[8] K. Ronaldson-Bouchard, S.P. Ma, K. Yeager, T. Chen, L. Song, D. Sirabella, K. Morikawa, D. Teles, M. Yazawa, G. Vunjak-Novakovic, Advanced maturation of human cardiac tissue grown from pluripotent stem cells, Nature 556 (7700) (2018) 239–243.

[9] J.C. Nawroth, L.L. Scudder, R.T. Halvorson, J. Tresback, J.P. Ferrier, S.P. Sheehy, A. Cho, S. Kannan, I. Sunyovszki, J.A. Goss, Automated fabrication of photopatterned gelatin hydrogels for organ-on-chips applications, Biofabrication 10 (2) (2018) 025004.

[10] M. Schubert, L. Woolfson, I.R. Barnard, A.M. Dorward, B. Casement, A. Morton, G.B. Robertson, P.L. Appleton, G.B. Miles, C.S. Tucker, Monitoring contractility in cardiac tissue with cellular resolution using biointegrated microlasers, Nat. Photonics 14 (7) (2020) 452–458.

[11] Z. Wang, S.J. Lee, H.-J. Cheng, J.J. Yoo, A. Atala, 3D bioprinted functional and contractile cardiac tissue constructs, Acta Biomater. 70 (2018) 48–56.

[12] J. Lee, V. Manoharan, L. Cheung, S. Lee, B.-H. Cha, P. Newman, R. Farzad, S. Mehrotra, K. Zhang, F. Khan, Nanoparticle-based hybrid scaffolds for deciphering the role of multimodal cues in cardiac tissue engineering, ACS Nano 13 (11) (2019) 12525–12539.

[13] N. Huebsch, B. Charrez, G. Neiman, B. Siemons, S.C. Boggess, S. Wall, V. Charwat, K.H. Jæger, D. Cleres, Å. Telle, Metabolically driven maturation of human-induced-pluripotent-stem-cell-derived cardiac microtissues on microfluidic chips, Nat. Biomed. Eng. 6 (4) (2022) 372–388.

[14] A.C. Daly, M.D. Davidson, J.A. Burdick, 3D bioprinting of high cell-density heterogeneous tissue models through spheroid fusion within self-healing hydrogels, Nat. Commun. 12 (1) (2021) 1–13.

[15] J. Veldhuizen, J. Cutts, D.A. Brafman, R.Q. Migrino, M. Nikkhah, Engineering anisotropic human stem cell-derived three-dimensional cardiac tissue on-a-chip, Biomaterials 256 (2020), 120195.

[16] K. Roshanbinfar, L. Vogt, F. Ruther, J.A. Roether, A.R. Boccaccini, F.B. Engel, Nanofibrous composite with tailorable electrical and mechanical properties for cardiac tissue engineering, Adv. Funct. Mater. 30 (7) (2020), 1908612.

[17] M. Miura, T. Handoh, Y. Taguchi, T. Hasegawa, Y. Takahashi, N. Morita, A. Matsumoto, C. Shindoh, H. Sato, Transient elevation of glucose increases arrhythmia susceptibility in non-diabetic rat trabeculae with non-uniform contraction, Circ. J. (2020). CJ-19-0715.

[18] E. Cohen, A. Agrawal, M. Connors, B. Hansen, H. Charkhkar, J. Pfefer, Optical coherence tomography imaging of retinal damage in real time under a stimulus electrode, J. Neural. Eng. 8 (5) (2011), 056017.

[19] S.F. Cogan, K.A. Ludwig, C.G. Welle, P. Takmakov, Tissue damage thresholds during therapeutic electrical stimulation, J. Neural. Eng. 13 (2) (2016), 021001.

[20] Y. Zhao, E.Y. Wang, L.H. Davenport, Y. Liao, K. Yeager, G. Vunjak-Novakovic, M. Radisic, B. Zhang, A multimaterial microphysiological platform enabled by rapid casting of elastic microwires, Adv. Healthcare Mater. 8 (5) (2019), 1801187.

[21] V.Y. Sidorov, P.C. Samson, T.N. Sidorova, J.M. Davidson, C.C. Lim, J.P. Wikswo, I-Wire Heart-on-a-Chip I: three-dimensional cardiac tissue constructs for physiology and pharmacology, Acta Biomater. 48 (2017) 68–78.

[22] K.S. Bielawski, A. Leonard, S. Bhandari, C.E. Murry, N.J. Sniadecki, Real-time force and frequency analysis of engineered human heart tissue derived from induced pluripotent stem cells using magnetic sensing, tissue engineering, Part C, Methods 22 (10) (2016) 932–940.

[23] U. Arslan, A. Moruzzi, J. Nowacka, C. Mummery, D. Eckardt, P. Loskill, V. Orlova, Microphysiological stem cell models of the human heart, Materials Today Bio (2022), 100259.

[24] N. Huebsch, P. Loskill, M.A. Mandegar, N.C. Marks, A.S. Sheehan, Z. Ma, A. Mathur, T.N. Nguyen, J.C. Yoo, L.M. Judge, Automated video-based analysis of contractility and calcium flux in human-induced pluripotent stem cell-derived cardiomyocytes cultured over different spatial scales, Tissue Eng. C Methods 21 (5) (2015) 467–479.

[25] A. Mathur, P. Loskill, K. Shao, N. Huebsch, S. Hong, S.G. Marcus, N. Marks, M. Mandegar, B.R. Conklin, L.P. Lee, Human iPSC-based cardiac microphysiological system for drug screening applications, Sci. Rep. 5 (1) (2015) 1–7.

[26] N. Thavandiran, C. Hale, P. Blit, M.L. Sandberg, M.E. McElvain, M. Gagliardi, B. Sun, A. Witty, G. Graham, V.T.H. Do, M.A. Bakooshli, H. Le, J. Ostblom, S. McEwen, E. Chau, A. Prowse, I. Fernandes, A. Norman, P.M. Gilbert, G. Keller, P. Tagari, H. Xu, M. Radisic, P.W. Zandstra, Functional arrays of human pluripotent stem cell-derived cardiac microtissues, Sci. Rep. 10 (1) (2020) 6919.

[27] Y. Zhao, N. Rafatian, N.T. Feric, B.J. Cox, R. Aschar-Sobbi, E.Y. Wang, P. Aggarwal, B. Zhang, G. Conant, K. Ronaldson-Bouchard, A. Pahnke, S. Protze, J.H. Lee, L. Davenport Huyer, D. Jekic, A. Wickeler, H.E. Naguib, G.M. Keller, G. Vunjak-Novakovic, U. Broeckel, P.H. Backx, M. Radisic, A platform for generation of chamber-specific cardiac tissues and disease modeling, Cell 176 (4) (2019) 913–927 e18.

[28] S.B. Campbell, Q. Wu, J. Yazbeck, C. Liu, S. Okhovatian, M. Radisic, Beyond polydimethylsiloxane: alternative materials for fabrication of organ-on-a-chip devices and microphysiological systems, ACS Biomater. Sci. Eng. 7 (7) (2020) 2880–2899.

[29] J. Lachaux, C. Alcaine, B. Gomez-Escoda, C.M. Perrault, D.O. Duplan, P.-Y.J. Wu, I. Ochoa, L. Fernández, O. Mercier, D. Coudreuse, Thermoplastic elastomer with advanced hydrophilization and bonding performances for rapid (30 s) and easy molding of microfluidic devices, Lab Chip 17 (15) (2017) 2581–2594.

[30] S.T. Selvan, T.T. Tan, J.Y. Ying, Robust, non-cytotoxic, silica-coated CdSe quantum dots with efficient photoluminescence, Adv. Mater. 17 (13) (2005) 1620–1625.

[31] Y. Cao, A. Stavrinadis, T. Lasanta, D. So, G. Konstantatos, The role of surface passivation for efficient and photostable PbS quantum dot solar cells, Nat. Energy 1 (4) (2016) 1–6.

[32] S. Ye, W. Yan, M. Zhao, X. Peng, J. Song, J. Qu, Low-saturation-intensity, high-photostability, and high-resolution STED nanoscopy assisted by CsPbBr3 quantum dots, Adv. Mater. 30 (23) (2018), 1800167.

[33] J. Cho, Y.K. Jung, J.-K. Lee, H.-S. Jung, Highly efficient blue-emitting CdSe-derived core/shell gradient alloy quantum dots with improved photoluminescent quantum yield and enhanced photostability, Langmuir 33 (15) (2017) 3711–3719.

[34] A. Benayas, F. Ren, E. Carrasco, V. Marzal, B. del Rosal, B.A. Gonfa, Á. Juarranz, F. Sanz-Rodríguez, D. Jaque, J. García-Solé, PbS/CdS/ZnS quantum dots: a multifunctional platform for in vivo near-infrared low-dose fluorescence imaging, Adv. Funct. Mater. 25 (42) (2015) 6650–6659.

[35] E.Y. Wang, J. Smith, M. Radisic, Design and fabrication of biological wires for cardiac fibrosis disease modeling, Methods Mol. Biol. 2485 (2022) 175–190.

[36] X. Lian, J. Zhang, S.M. Azarin, K. Zhu, L.B. Hazeltine, X. Bao, C. Hsiao, T.J. Kamp, S.P. Palecek, Directed cardiomyocyte differentiation from human pluripotent stem cells by modulating Wnt/β-catenin signaling under fully defined conditions, Nat. Protoc. 8 (1) (2013) 162.

[37] L. Yang, M.H. Soonpaa, E.D. Adler, T.K. Roepke, S.J. Kattman, M. Kennedy, E. Henckaerts, K. Bonham, G.W. Abbott, R.M. Linden, Human cardiovascular progenitor cells develop from a KDR+ embryonic-stem-cell-derived population, Nature 453 (7194) (2008) 524.

[38] L. Davenport Huyer, A.D. Bannerman, Y. Wang, H. Savoji, E.J. Knee-Walden, A. Brissenden, B. Yee, M. Shoaib, E. Bobicki, B.G. Amsden, One-pot synthesis of unsaturated polyester bioelastomer with controllable material curing for microscale designs, Adv. Healthcare Mater. 8 (16) (2019), 1900245.

[39] L. Davenport Huyer, B. Zhang, A. Korolj, M. Montgomery, S. Drecun, G. Conant, Y. Zhao, L. Reis, M. Radisic, Highly elastic and moldable polyester biomaterial for cardiac tissue engineering applications, ACS Biomater. Sci. Eng. 2 (5) (2016) 780–788.

[40] Q. Wu, P. Zhang, G. O'Leary, Y. Zhao, Y. Xu, N. Rafatian, S. Okhovatian, S. Landau, T.A. Valiante, J. Travas-Sejdic, Flexible 3D printed microwires and 3D

microelectrodes for heart-on-a-chip engineering, Biofabrication 15 (3) (2023), 035023.

[41] E.Y. Wang, J. Smith, M. Radisic, Design and fabrication of biological WiresBiological wires for cardiac FibrosisFibrosis disease modeling, in: K.L. K. Coulombe, L.D. Black Iii (Eds.), Cardiac Tissue Engineering: Methods and Protocols, Springer US, New York, NY, 2022, pp. 175–190.

[42] N. Thavandiran, N. Dubois, A. Mikryukov, S. Masse, B. Beca, C.A. Simmons, V. S. Deshpande, J.P. McGarry, C.S. Chen, K. Nanthakumar, G.M. Keller, M. Radisic, P.W. Zandstra, Design and formulation of functional pluripotent stem cell-derived cardiac microtissues, Proc. Natl. Acad. Sci. U.S.A. 110 (49) (2013) E4698–E4707.

[43] J. Kramer, C.A. Obejero-Paz, G. Myatt, Y.A. Kuryshev, A. Bruening-Wright, J. S. Verducci, A.M. Brown, MICE models: superior to the HERG model in predicting Torsade de Pointes, Sci. Rep. 3 (1) (2013) 2100.

[44] F. Wang, M. Koide, G.C. Wellman, Nifedipine inhibition of high-voltage activated calcium channel currents in cerebral artery myocytes is influenced by extracellular divalent cations, Front. Physiol. 8 (2017) 210.

[45] K.H. Jæger, V. Charwat, B. Charrez, H. Finsberg, M.M. Maleckar, S. Wall, K. E. Healy, A. Tveito, Improved computational identification of drug response using optical measurements of human stem cell derived cardiomyocytes in microphysiological systems, Front. Pharmacol. 10 (2020) 1648.

[46] J.K. Gibson, Y. Yue, J. Bronson, C. Palmer, R. Numann, Human stem cell-derived cardiomyocytes detect drug-mediated changes in action potentials and ion currents, J. Pharmacol. Toxicol. Methods 70 (3) (2014) 255–267.

[47] P.B. Bennett, C. Valenzuela, L.-Q. Chen, R.G. Kallen, On the molecular nature of the lidocaine receptor of cardiac Na+ channels: modification of block by alterations in the α-subunit III-IV interdomain, Circ. Res. 77 (3) (1995) 584–592.

[48] O. Sirenko, C. Crittenden, N. Callamaras, J. Hesley, Y.-W. Chen, C. Funes, I. Rusyn, B. Anson, E.F. Cromwell, Multiparameter in vitro assessment of compound effects on cardiomyocyte physiology using iPSC cells, J. Biomol. Screen 18 (1) (2013) 39–53.

[49] L.M. Hesketh, M.B. Sikkel, L. Mahoney-Sanchez, F. Mazzacuva, R.A. Chowdhury, K. N. Tzortzis, J. Firth, J. Winter, K.T. MacLeod, S. Ogrodzinski, OCT2013, an ischaemia-activated antiarrhythmic prodrug, devoid of the systemic side effects of lidocaine, Br. J. Pharmacol. 179 (9) (2022) 2037–2053.

[50] J. Schwan, A.T. Kwaczala, T.J. Ryan, O. Bartulos, Y. Ren, L.R. Sewanan, A. H. Morris, D.L. Jacoby, Y. Qyang, S.G. Campbell, Anisotropic engineered heart tissue made from laser-cut decellularized myocardium, Sci. Rep. 6 (1) (2016) 1–12.

[51] M. Riaz, J. Park, L.R. Sewanan, Y. Ren, J. Schwan, S.K. Das, P.T. Pomianowski, Y. Huang, M.W. Ellis, J. Luo, Muscle LIM protein force-sensing mediates sarcomeric biomechanical signaling in human familial hypertrophic cardiomyopathy, Circulation 145 (16) (2022) 1238–1253.

[52] R. Ng, L.R. Sewanan, P. Stankey, X. Li, Y. Qyang, S. Campbell, Shortening velocity causes myosin isoform shift in human engineered heart tissues, Circ. Res. 128 (2) (2021) 281–283.

[53] J.H. Tsui, A. Leonard, N.D. Camp, J.T. Long, Z.Y. Nawas, R. Chavanachat, A. S. Smith, J.S. Choi, Z. Dong, E.H. Ahn, Tunable electroconductive decellularized extracellular matrix hydrogels for engineering human cardiac microphysiological systems, Biomaterials 272 (2021), 120764.

[54] K.S. Bielawski, A. Leonard, S. Bhandari, C.E. Murry, N.J. Sniadecki, Real-time force and frequency analysis of engineered human heart tissue derived from induced pluripotent stem cells using magnetic sensing, Tissue Eng. C Methods 22 (10) (2016) 932–940.

[55] S. Lee, V. Serpooshan, X. Tong, S. Venkatraman, M. Lee, J. Lee, O. Chirikian, J. C. Wu, S.M. Wu, F. Yang, Contractile force generation by 3D hiPSC-derived cardiac tissues is enhanced by rapid establishment of cellular interconnection in matrix with muscle-mimicking stiffness, Biomaterials 131 (2017) 111–120.

[56] B.J. Van Meer, A. Krotenberg, L. Sala, R.P. Davis, T. Eschenhagen, C. Denning, L. G. Tertoolen, C.L. Mummery, Simultaneous measurement of excitation-contraction coupling parameters identifies mechanisms underlying contractile responses of hiPSC-derived cardiomyocytes, Nat. Commun. 10 (1) (2019) 1–9.

[57] S.-Y. Lee, D.-S. Kim, E.-S. Kim, D.-W. Lee, Nano-textured polyimide cantilever for enhancing the contractile behavior of cardiomyocytes and its application to cardiac toxicity screening, Sensor. Actuator. B Chem. 301 (2019), 126995.

[58] J.U. Lind, T.A. Busbee, A.D. Valentine, F.S. Pasqualini, H. Yuan, M. Yadid, S.-J. Park, A. Kotikian, A.P. Nesmith, P.H. Campbell, Instrumented cardiac

[59] microphysiological devices via multimaterial three-dimensional printing, Nat. Mater. 16 (3) (2017) 303–308.

[59] G. Wang, M.L. McCain, L. Yang, A. He, F.S. Pasqualini, A. Agarwal, H. Yuan, D. Jiang, D. Zhang, L. Zangi, J. Geva, A.E. Roberts, Q. Ma, J. Ding, J. Chen, D. Z. Wang, K. Li, J. Wang, R.J. Wanders, W. Kulik, F.M. Vaz, M.A. Laflamme, C. E. Murry, K.R. Chien, R.I. Kelley, G.M. Church, K.K. Parker, W.T. Pu, Modeling the mitochondrial cardiomyopathy of Barth syndrome with induced pluripotent stem cell and heart-on-chip technologies, Nat. Med. 20 (6) (2014) 616–623.

[60] A.W. Feinberg, A. Feigel, S.S. Shevkoplyas, S. Sheehy, G.M. Whitesides, K. K. Parker, Muscular thin films for building actuators and powering devices, Science 317 (5843) (2007) 1366–1370.

[61] S.P. Sheehy, F. Pasqualini, A. Grosberg, S.J. Park, Y. Aratyn-Schaus, K.K. Parker, Quality metrics for stem cell-derived cardiac myocytes, Stem Cell Rep. 2 (3) (2014) 282–294.

[62] J.D. Wang, N.J. Douville, S. Takayama, M. ElSayed, Quantitative analysis of molecular absorption into PDMS microfluidic channels, Ann. Biomed. Eng. 40 (9) (2012) 1862–1873.

[63] K. Domansky, J.D. Sliz, N. Wen, C. Hinojosa, G. Thompson, J.P. Fraser, T. Hamkins-Indik, G.A. Hamilton, D. Levner, D.E. Ingber, SEBS elastomers for fabrication of microfluidic devices with reduced drug absorption by injection molding and extrusion, Microfluid. Nanofluidics 21 (2017) 1–12.

[64] S.B. Campbell, Q. Wu, J. Yazbeck, C. Liu, S. Okhovatian, M. Radisic, Beyond polydimethylsiloxane: alternative materials for fabrication of organ-on-a-chip devices and microphysiological systems, ACS Biomater. Sci. Eng. 7 (7) (2021) 2880–2899.

[65] Y. Zhao, E.Y. Wang, L.H. Davenport, Y. Liao, K. Yeager, G. Vunjak-Novakovic, M. Radisic, B. Zhang, A multimaterial microphysiological platform enabled by rapid casting of elastic microwires, Adv. Healthcare Mater. 8 (5) (2019), e1801187.

[66] J.P. Kim, Z. Xie, M. Creer, Z. Liu, J. Yang, Citrate-based fluorescent materials for low-cost chloride sensing in the diagnosis of cystic fibrosis, Chem. Sci. 8 (1) (2017) 550–558.

[67] D. Shan, J.T. Hsieh, X. Bai, J. Yang, Citrate-based fluorescent biomaterials, Adv. Healthcare Mater. 7 (18) (2018), 1800532.

[68] Z. Xie, J.P. Kim, Q. Cai, Y. Zhang, J. Guo, R.S. Dhami, L. Li, B. Kong, Y. Su, K. A. Schug, Synthesis and characterization of citrate-based fluorescent small molecules and biodegradable polymers, Acta Biomater. 50 (2017) 361–369.

[69] Q. Wu, P. Zhang, G. O'Leary, Y. Zhao, Y. Xu, N. Rafatian, S. Okhovatian, S. Landau, T.A. Valiante, J. Travas-Sejdic, M. Radisic, Flexible 3D printed microwires and 3D microelectrodes for heart-on-a-chip engineering, Biofabrication 15 (3) (2023).

[70] Y. Zhao, N. Rafatian, E.Y. Wang, N.T. Feric, B.F. Lai, E.J. Knee-Walden, P.H. Backx, M. Radisic, Engineering microenvironment for human cardiac tissue assembly in heart-on-a-chip platform, Matrix Biol. 85 (2020) 189–204.

[71] N. Thavandiran, N. Dubois, A. Mikryukov, S. Massé, B. Beca, C.A. Simmons, V. S. Deshpande, J.P. McGarry, C.S. Chen, K. Nanthakumar, Design and formulation of functional pluripotent stem cell-derived cardiac microtissues, Proc. Natl. Acad. Sci. USA 110 (49) (2013) E4698–E4707.

[72] N. Huebsch, P. Loskill, N. Deveshwar, C.I. Spencer, L.M. Judge, M.A. Mandegar, C. B Fox, T. Mohamed, Z. Ma, A. Mathur, Miniaturized iPS-cell-derived cardiac muscles for physiologically relevant drug response analyses, Sci. Rep. 6 (1) (2016) 1–12.

[73] L.A. MacQueen, S.P. Sheehy, C.O. Chantre, J.F. Zimmerman, F.S. Pasqualini, X. Liu, J.A. Goss, P.H. Campbell, G.M. Gonzalez, S.-J. Park, A tissue-engineered scale model of the heart ventricle, Nat. Biomed. Eng. 2 (12) (2018) 930–941.

[74] M.H. Mohammadi, S. Okhovatian, H. Savoji, S.B. Campbell, B.F.L. Lai, J. Wu, S. Pascual-Gil, D. Bannerman, N. Rafatian, R.K. Li, M. Radisic, Toward hierarchical assembly of aligned cell sheets into a conical cardiac ventricle using microfabricated elastomers, Adv Biol (Weinh) 6 (11) (2022), e2101165.

[75] A. Lee, A. Hudson, D. Shiwarski, J. Tashman, T. Hinton, S. Yerneni, J. Bliley, P. Campbell, A. Feinberg, 3D bioprinting of collagen to rebuild components of the human heart, Science 365 (6452) (2019) 482–487.

[76] S. Okhovatian, M.H. Mohammadi, N. Rafatian, M. Radisic, Engineering models of the heart left ventricle, ACS Biomater. Sci. Eng. 8 (6) (2022) 2144–2160.